



Identification and Spectroscopic Characterization of 128 New Herbig Stars*

Miguel Vioque^{1,2,3}, René D. Oudmaijer³, Chumpon Wichittanakom^{3,4}, Ignacio Mendigutía⁵, Deborah Baines⁶,Olja Panić³, Daniela Iglesias³, James Miley^{1,7}, and Ricardo Pérez-Martínez⁸¹ Joint ALMA Observatory, Alonso de Córdova 3107, Vitacura, Santiago 763-0355, Chile; miguel.vioque@alma.cl² National Radio Astronomy Observatory, 520 Edgemont Road, Charlottesville, VA 22903, USA³ School of Physics and Astronomy, Sir William Henry Bragg Building, University of Leeds, Leeds LS2 9JT, UK⁴ Department of Physics, Faculty of Science and Technology, Thammasat University, Rangsit Campus, Pathum Thani 12120, Thailand⁵ Centro de Astrobiología (CSIC-INTA), Departamento de Astrofísica, ESA-ESAC Campus, E-28691 Madrid, Spain⁶ Quasar Science Resources for ESA-ESAC, ESAC Science Data Centre, PO Box 78, E-28691 Villanueva de la Cañada, Madrid, Spain⁷ National Astronomical Observatory of Japan, Alonso de Córdova 3788, 61B Vitacura, Santiago, Chile⁸ Ingeniería de Sistemas para la Defensa de España (Isdefe) for ESA-ESAC, PO Box 78, E-28691 Villanueva de la Cañada, Madrid, Spain

Received 2022 January 1; revised 2022 March 2; accepted 2022 March 2; published 2022 May 3

Abstract

We present optical spectroscopy observations of 145 high-mass pre-main-sequence candidates from the catalog of Vioque et al. 2020. From these, we provide evidence for the Herbig nature of 128 sources. This increases the number of known objects of the class by $\sim 50\%$. We determine the stellar parameters of these sources using the spectra and Gaia EDR3 data. The new sources are well distributed in mass and age, with 23 sources between 4 and $8 M_{\odot}$ and 32 sources above $8 M_{\odot}$. Accretion rates are inferred from $H\alpha$ and $H\beta$ luminosities for 104 of the new Herbig stars. These accretion rates, combined with previous similar estimates, allow us to analyze the accretion properties of Herbig stars using the largest sample ever considered. We provide further support to the existence of a break in accretion properties at $\sim 3\text{--}4 M_{\odot}$, which was already reported for the previously known Herbig stars. We re-estimate the potential break in accretion properties to be at $3.87^{+0.38}_{-0.96} M_{\odot}$. As observed for the previously known Herbig stars, the sample of new Herbig stars independently suggests intense inner-disk photoevaporation for sources with masses above $\sim 7 M_{\odot}$. These observations provide robust observational support to the accuracy of the Vioque et al. 2020 catalog of Herbig candidates.

Unified Astronomy Thesaurus concepts: Herbig Ae/Be stars (723); Star formation (1569); Pre-main sequence stars (1290); Young stellar objects (1834); Massive stars (732); Stellar accretion (1578); Hertzsprung Russell diagram (725); Emission line stars (460)

Supporting material: machine-readable tables

1. Introduction

The group of intermediate- to high-mass pre-main-sequence (PMS) sources ($M > 1.5 M_{\odot}$) play a particularly important part in understanding the differences in the formation of, and accretion of matter onto, low- and high-mass stars. Whereas the formation of low-mass stars is widely accepted to be due to magnetically controlled accretion (Bouvier et al. 2007), higher mass stars are generally non-magnetic, and it would be expected that this scenario does not apply to them (see Mendigutía 2020). Recent studies (e.g., Wichittanakom et al. 2020; Grant et al. 2022) have provided evidence for the change in accretion mechanism happening at around $4 M_{\odot}$.

In addition, the protoplanetary disks of intermediate- to high-mass PMS stars show significant differences with respect to the disks around low-mass stars. The more luminous stars promptly photoevaporate their inner disks with FUV photons (Kunitomo et al. 2021), causing large inner cavities. The

impact this has on the thermal and chemical evolution of the disks may significantly impact the formation and evolution of planets (Panić & Min 2017; Miley et al. 2021). Mm-wavelength observations have also shown that the disks around intermediate-mass stars are more massive than those around low-mass stars (Andrews et al. 2013; Pascucci et al. 2016; Stapper et al. 2022) and have a higher fraction of detected structures in the dust disk (van der Marel & Mulders 2021; Stapper et al. 2022). Furthermore, there is evidence pointing toward particular disk structures being favored in more massive objects (e.g., spirals have been mostly found in early spectral type stars, Garufi et al. 2018). Hence, it has been theorized that they have a higher incidence of giant planets (e.g., Reffert et al. 2015; van der Marel et al. 2021). Therefore, the disks around intermediate- to high-mass PMS stars play a key role for understanding the structures and evolution processes of protoplanetary disks, and their link to planet formation.

The intermediate- to high-mass PMS regime comprises different types of young stellar objects (YSOs). The Herbig Ae/Be group contains stars at the latest stages of pre-main-sequence evolution. In total, around 255 Herbig Ae/Be sources have been historically considered and studied (e.g., Vioque et al. 2018), although a smaller fraction has been properly characterized and is free of contaminants (see the seminal papers of Thé et al. 1994; Vieira et al. 2003, and Hernández et al. 2004). Recent compilations and studies about the general properties of Herbig Ae/Be stars can be found in Vioque et al. (2018) and

* Based on observations collected at the European Southern Observatory (ESO) under ESO program 0104.C-0937(A) and 0104.C-0937(B), observations made in the Observatorios de Canarias del IAC, program 103-INT13/19B, and observations collected at the Centro Astronómico Hispano-Alemán (CAHA) at Calar Alto from 2019-04-Sept to 2019-06-Sept.

Table 1

Observing Dates and Instrumental Setups for the Three Observing Runs; Including Telescope, Spectrograph, CCD Detector, Grating or Grism Used, Spectral Range in Å, Reciprocal Dispersion in Å/pixel, and Spectral Resolution in Å

Date Ranges	Telescope	Instrument	Detector	Grating/Grism	Range (Å)	Dispersion (Å pixel ⁻¹)	Resolution (Å)	Number of Sources
4–7 Aug 2019	INT	IDS	EEV10	R900V	3600–5000	0.63	~1.3	56
8–11 Aug 2019	INT	IDS	RED+2	R1200R	5700–6700	0.52	~1.0	56
3–5 Sep 2019	CAHA2.2m	CAFOS	SITe-1d	B-100	3200–5800	2.0	~4.0	39
11–13 Mar 2020	NTT	EFOSC2	CCD#40	G7	3300–5300	0.96	~7.4	50
17–20 Mar 2020	NTT	EFOSC2	CCD#40	G20	6000–7200	0.55	~3.5	48

Note. The signal-to-noise ratio of these spectra are typically in the order of 100. A total of 145 different sources were observed.

Guzmán-Díaz et al. (2021). The cooler predecessors of the Herbig Ae/Be stars are occasionally referred to as Intermediate-Mass T Tauris (IMTTs). The defining difference between both groups is arbitrary in the literature and different thresholds in spectral type and mass have been used (e.g., Calvet et al. 2004; Povich et al. 2016; Villebrun et al. 2019; Nuñez et al. 2021; Valegård et al. 2021). Valegård et al. (2021) compiled most IMTTs within 500 pc, describing the general properties of a sample of 49 sources. Higher-mass PMS objects ($M > 8\text{--}10 M_{\odot}$) are generally called Massive Young Stellar Objects (MYSOs). However, the difference between the former two categories and the MYSOs is also ambiguous, often depending on the optical visibility of the sources. The most comprehensive catalog of MYSOs to date can be found in Lumsden et al. (2013) with several hundred sources, although only a very small fraction of those have been characterized in great detail (e.g., Frost et al. 2021; Koumpia et al. 2021).

A large caveat of all the aforementioned results is that there is no homogeneous or complete survey of intermediate- to high-mass PMS stars. The existing samples are small heterogeneous collections of often randomly discovered objects, with a non-negligible amount of contaminants. This is a direct consequence of the Initial Mass Function (IMF): there are few nearby high-mass stars in any given molecular cloud (e.g., there are three stars with $M > 1.5 M_{\odot}$ in the ALMA survey of Lupus, Ansdell et al. 2016). Any global conclusions that have been drawn are therefore subject to an unknown bias. Furthermore, as more massive stars evolve faster, the younger, high-mass PMS stars have been barely considered by the vast majority of studies (e.g., in the samples of van der Marel et al. 2021 and Stapper et al. 2022 all sources are older than ~ 4 Myr). This has important consequences on the conclusions obtained so far for these objects. For example, at those late stages, planet formation is mostly over in the low-mass regime (Cieza et al. 2021), so it is probable that in general we have not been tracing actively planet-forming stars.

To properly investigate the evolution of intermediate- and high-mass PMS stars, what is needed is a well-selected sample covering a large range in age and mass. Vioque et al. (2020) produced a large homogeneous catalog of a few thousand intermediate- to high-mass PMS (“Herbig star”⁹) candidates by combining large-scale photometric surveys (Gaia, 2MASS, WISE, IPHAS, and VPHAS+; covering from the optical to the mid-IR and including H α photometry) with machine-learning techniques.

⁹ In this work, we call all YSOs with masses above $1.5 M_{\odot}$ “Herbig stars”. We elected this nomenclature because most of the sources identified and described in this work clearly belong to the Herbig Ae/Be group, although some others might better fit within the IMTTs or MYSOs regimes.

In this paper, we present spectroscopic observations for 145 Herbig candidates from the catalog of Vioque et al. (2020). We discuss the results of the observations and present a comprehensive list of 128 newly confirmed Herbig detections. We start the paper with a description of the observations in Section 2. For each observed object, we characterize the extinction and the stellar parameters in Section 3. After discarding some contaminants in Section 4, in Section 5 we present accretion rates for the fraction of the sources with H α or H β emission line measurements. In Section 6 the Herbig nature of the observed sources is assessed. In Section 7 the derived accretion rates are analyzed, and we compare them with the accretion rates of previously known Herbig stars. We discuss our results in Section 8 and conclude in Section 9.

2. Observations

A total of 145 Herbig candidates from the Vioque et al. (2020) catalog were observed in low- to medium-resolution optical spectroscopy during three different observing runs. Hence, this is a pilot study of the large catalog of 2226 intermediate- to high-mass PMS candidates of Vioque et al. (2020), only counting those sources with $\sigma(\varpi)/\varpi \leq 0.2$. These 145 sources were selected because their absolute magnitudes suggest that their stellar masses cover the Herbig mass regime in a representative manner. In order to obtain precise stellar parameters, we targeted sources with accurate parallaxes (ϖ , all but five have $\sigma(\varpi)/\varpi \leq 0.1$). This is because the parallax error dominates the uncertainty of the stellar parameters when these are obtained from the locations of the objects in the HR diagram (see, e.g., Vioque et al. 2018).

The signal-to-noise ratio of these spectra are typically on the order of 100. Observing dates and instrumental setups are detailed in Table 1. The three observing runs can be summarized as follows:

1. 56 Herbig candidates were observed with the Intermediate Dispersion Spectrograph (IDS) instrument which is at the Cassegrain focus of the 2.54 m Isaac Newton Telescope (INT). The INT is located at the Roque de los Muchachos Observatory in the island of La Palma, Spain. Two different configurations were used. One block used the R900V diffraction grating, which covers the $\sim 3600\text{--}5000$ Å spectral range. The other block used the R1200R grating ($\sim 5700\text{--}6700$ Å).
2. 39 Herbig candidates were observed with the Calar Alto Faint Object Spectrograph (CAFOS) at the RC focus of the Calar Alto 2.2 m telescope (CAHA2.2m) in Calar Alto Observatory, Spain. We employed the B-100 grism ($\sim 3200\text{--}5800$ Å).

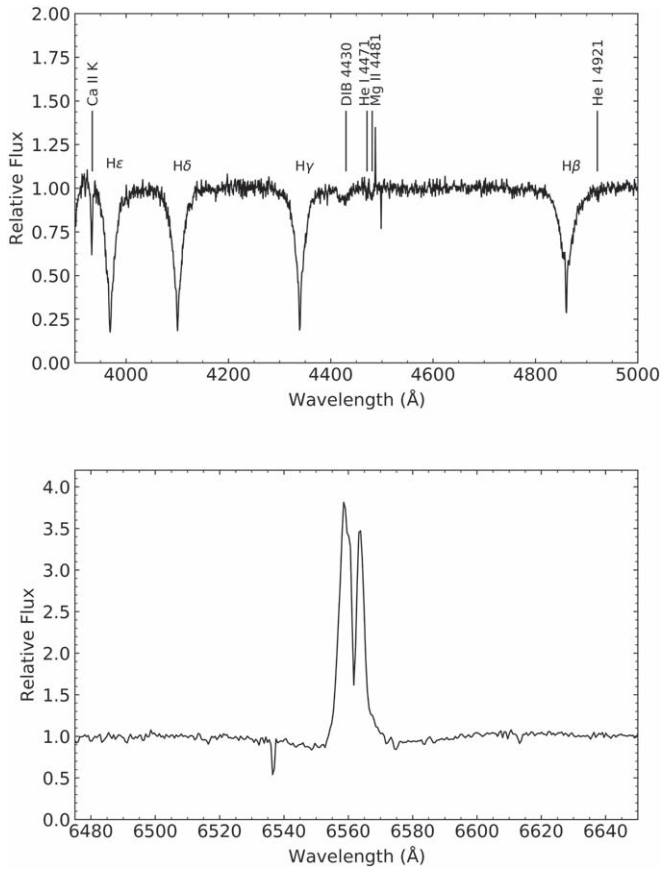


Figure 1. Example normalized spectra of VOS 140 (spectral type B9.5), observed at INT. Top: blue spectral range covered by our observations. Bottom: portion of the red spectral range covered by our observations centered around the H α line.

3. 50 Herbig candidates were observed with the ESO Faint Object Spectrograph and Camera (v.2) or EFOSC2 in two settings. EFOSC2 is installed at the Nasmyth B focus of the 3.58 m New Technology Telescope (NTT) at La Silla Observatory, Chile. The first block used the G7 diffraction grism ($\sim 3300\text{--}5300$ Å) and the second block used the G20 grism ($\sim 6000\text{--}7200$ Å).

A log of the observations is presented in Table B1. Bias, flat and arc frames were taken each night for the reduction of the observations. Standard procedures were used in order to process the data, which was reduced using the Image Reduction and Analysis Facility (IRAF). We started with bias subtraction. Next, flat-field division was used to correct the pixel-to-pixel variation of the CCD signal. Then, one-dimensional spectra were extracted and sky subtracted from science frames. Last, arc frames of Cu–Ar and Cu–Ne comparison lamps were used to obtain the wavelength calibrated normalized spectra.

2.1. Comments on the Blue Spectral Range

The blue spectral region considered in the three observing runs ($\sim 3300\text{--}5400$ Å) covers the main wavelength range to determine spectral types. An example of the normalized spectra obtained in this region is shown in Figure 1. This region is especially useful for the earlier spectral type stars such as A and B stars, as their spectrum in the wavelength range beyond 5000 Å is fairly line free. This region also covers the H β line, which is a common tracer of circumstellar activity in YSOs.

The chosen grisms allow for efficiently obtaining spectral types and effective temperatures (T_{eff}). These are tabulated in Table B2. For some objects, the temperature was estimated directly from model-fitting the spectra (see Wichittanakom et al. 2020). Otherwise spectral types were obtained by comparison with model spectra (BOSZ models, Bohlin et al. 2017) and published spectral standards (Digital Atlas by Gray¹⁰), and the T_{eff} in Table B2 are the values that correspond to those spectral types according to Pecaut & Mamajek (2013). In this latter case, the T_{eff} uncertainties are of one sub-spectral type. The procedure followed for each object is detailed in Table B2. T_{eff} could not be estimated for VOS 2164 and VOS 603 because of strong emission line spectra (see Section 4). “VOS” names refer to sources from the catalog of Vioque, Oudmaijer, Schreiner, et al. (2020).

2.2. Comments on the Red Spectral Range

At the INT and NTT telescopes, additional observations at a higher resolution were performed for each source, covering a redder spectral range ($\sim 5800\text{--}7000$ Å). The exceptions to this are VOS 50 and VOS 4463 (i.e., 104 sources in total, see Table 1). This red range covers the important diagnostic H α line, which enables the determination of accretion rates. An example of the normalized spectra obtained in this region around the H α line is shown in Figure 1.

The measured H α equivalent widths (EW_{obs} , observed above the continuum) are tabulated in Table B3. The H α line profile was classified into single-peaked, double-peaked, or P-Cygni profile (regular or inverse), following the classification scheme of Vioque et al. (2018). In addition, in Table B3, we state whether the H β line covered in the blue range (Section 2.1) appears in emission.

3. Stellar Parameters

In this section we use the Gaia Early Data Release 3 (EDR3, Gaia Collaboration et al. 2016, 2021) to derive the stellar luminosity of the observed sources and place them in the Hertzsprung Russell (HR) diagram. The HR diagram in combination with theoretical tracks provide us with estimations of the sources’ stellar mass and age.

3.1. Data Acquisition and Calibration

We obtained EDR3 source identifications by using the DR2 source identifications provided in Vioque et al. (2020) and the *gaiaedr3.dr2_neighbourhood* table of the Gaia Archive (see Torra et al. 2021).

The EDR3 parallax (Lindgren et al. 2021a) to distance conversion was done as follows. For the 140 sources with $\sigma(\varpi)/\varpi \leq 0.1$ we obtained the distance by simple inversion of the parallax. For the five sources with $0.1 < \sigma(\varpi)/\varpi \leq 1$, we used the geometric prior of Bailer-Jones et al. (2021). In all cases, the correction to the zero-point parallax bias of Lindgren et al. (2021b) was applied. To trace problematic parallaxes that may lead to spurious or heavily inaccurate distances, we used the *Fidelity* parameter of Rybizki et al. (2022). Only three observed sources have fidelities below 90% (VOS 1385, VOS 1440, and VOS 2158).

The Gaia photometry of the sources (described in Riello et al. 2021) is presented in Table B1. To obtain the Gaia EDR3

¹⁰ <https://ned.ipac.caltech.edu/level5/Gray/frames.html>

intrinsic $G_{BP}-G_{RP}$ colors of the observed sources, we converted the intrinsic Johnson–Cousins colors for dwarf stars of Pecaut & Mamajek (2013) to Gaia $G_{BP}-G_{RP}$ colors with the polynomial equation presented in Table C.2 of Riello et al. (2021). In order to evaluate the validity of this approach, we compared the intrinsic colors derived this way with those obtained from GALAH+ spectra (Casagrande et al. 2021, see their Figure 3), from RAVE DR6 data (Steinmetz et al. 2020) and from the Tycho-2 Spectral Type Catalogue (Wright et al. 2003). The correspondence in all cases is within the 0.03 mag error.

Extinctions were obtained using the effective temperatures (derived in Section 2.1), the intrinsic colors, and the color-dependent extinction coefficients of Casagrande et al. (2021), see their Figure 1). In all cases $R_V = 3.1$ was assumed. The median error for the derived A_V values is 0.17 mag.

By fitting an atmosphere model from Castelli & Kurucz (2003) of the corresponding T_{eff} to the de-reddened Gaia G_{RP} photometry we derive the total stellar flux for each source. Combining this flux with the distance we obtain the total luminosity (L , in a procedure similar to that of Vioque et al. 2018). We have assumed solar metallicity and $\log(g) = 4.0$. The effect of these parameters in the derived luminosities is negligible.

The luminosities of all sources are presented in Table B2, together with their distances and A_V extinctions.

3.2. SEDs and IR Excess

Fitting an atmosphere model to the de-reddened photometry (Section 3.1) allows us to generate Spectral Energy Distributions (SED) to estimate the amount of infrared (IR) excess. For doing this, we use the 2MASS and WISE passbands (from AllWISE, Cutri et al. 2013) which are available for all sources (see Vioque et al. 2020). These passbands range from J band ($1.24 \mu\text{m}$) to $W4$ band ($22 \mu\text{m}$). The derived IR excesses (L_{IR}/L_*) appear tabulated in Table B3.

We note that WISE bands, especially W3 ($12 \mu\text{m}$) and W4, have a point-spread function that might lead to contaminated photometry in crowded regions or with bright backgrounds (see e.g., Koenig & Leisawitz 2014; Ribas et al. 2014). In general, the IR excesses derived this way should be considered as indicative, as a fraction of them might be affected by this caveat. A warning flag was included in the Vioque et al. (2020) catalog indicating potential problematic W3 and W4 passbands. In Table B3, this warning flag has been refined by examining the images at W1, W2, W3, and W4 as a set. In total, we found 29 sources where contamination is suspected.

There are six sources (VOS 76, VOS 78, VOS 491, VOS 1240, VOS 1385, and VOS 2161) with an IR excess over 70% of the stellar bolometric luminosity ($L_{\text{IR}}/L_* > 0.7$), which is the maximum excess typically observed in Herbig stars (e.g., Pascual et al. 2016; Banzatti et al. 2018). This implies that the IR excess luminosity of those sources likely includes a large amount of contamination from extended background emission.

3.3. Hertzsprung Russell Diagram

We present the 143 observed sources with T_{eff} determinations in an HR diagram in Figure 2. From this HR diagram, we derive masses and ages by using the PARSEC 1.2S pre-main-sequence tracks (Bressan et al. 2012; Marigo et al. 2017). These masses and ages are tabulated in Table B2. We note that

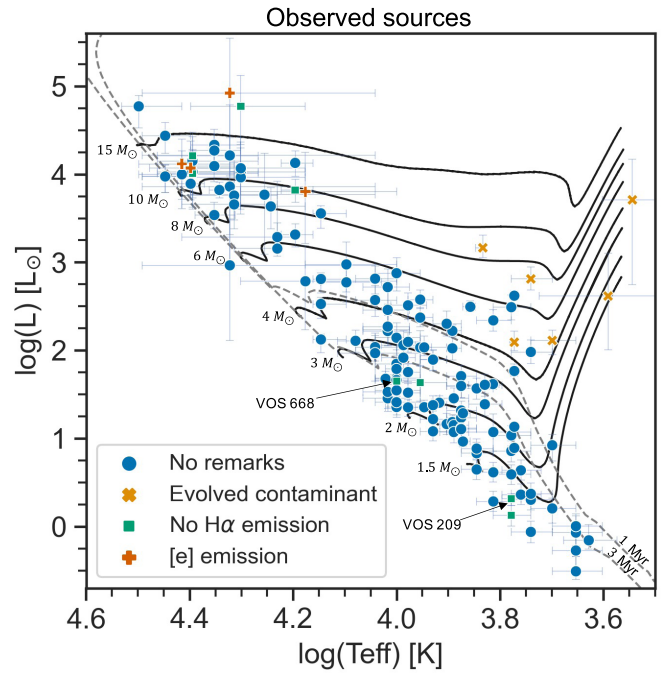


Figure 2. HR diagram of the 143 stars observed with T_{eff} determinations. The sources with a remark are discussed in Section 4 and Appendix A. PARSEC 1.2S PMS tracks and isochrones corresponding to 1.5, 2, 3, 4, 6, 8, 10, 15 M_{\odot} and 1 and 3 Myr are presented (Bressan et al. 2012 and Marigo et al. 2017).

the ages are very model dependent, are based on an arbitrary decision of the age “zero,” and are very susceptible to the HR diagram location uncertainties.

There are nine sources which are inconsistent with masses $M > 1.5 M_{\odot}$. Therefore, they rather belong to the T Tauri regime. These are highlighted in Table B2. The remaining 134 sources are compatible with the Herbig regime ($M > 1.5 M_{\odot}$).

4. Contaminants

The spectral analysis of Section 2 and the derivations of Section 3 allow us to identify some evolved contaminants among the observed PMS candidates. VOS 1634 and VOS 1806 have spectral types corresponding to an M and a K star, respectively. Their Gaia EDR3 parallaxes assign them luminosities over $400 L_{\odot}$. Hence, these are probably post-MS giants rather than PMS sources, as YSOs this massive would not be optically visible at such early stages of evolution. VOS 2164 spectra clearly correspond to a planetary nebula (and it appears as so in previous literature; e.g., Kaler et al. 1976). In addition, previous literature allowed us to identify VOS 603 as a cataclysmic variable star (dwarf nova; e.g., Otulakowska-Hypka et al. 2016), VOS 1240 as a carbon star (e.g., Groenewegen et al. 2002), VOS 1380 as a Type II Cepheid (e.g., Schmidt et al. 2004), and VOS 1385 as a RV Tau variable (Braga et al. 2018). VOS 458 was identified as an AGB candidate in Robitaille et al. (2008). However, it is a bit hot and under-luminous for an AGB star. We included VOS 458 in the list of contaminants because of its uncertain nature, although we note that the stellar parameters derived for VOS 458 are not incompatible with a YSO nature.

In total, we have identified eight evolved stars within the 145 observed PMS candidates. These appear marked in the HR diagram of Figure 2 and are removed from the rest of the

analysis. Hence, the number of observed sources we consider in what follows is 137 (145–8).

We should point out that separating Herbig stars from classical Be stars (very similar emission line non-PMS sources, Rivinius et al. 2013) was the main task of the machine-learning algorithm used in Vioque et al. (2020). Hence, the sample observed in this work is already filtered of classical Be stars.

5. Mass Accretion Rates

For the sources with $H\alpha$ and $H\beta$ lines in emission we corrected the measured EWs for the underlying line absorption. To do this we used the typical EW absorption values of each spectral subtype (Joner & Hintz 2015). These corrected equivalent widths (EW_{cor}) are tabulated in Table B3, together with the observed ones (EW_{obs}). Following, for example, Fairlamb et al. (2017): $F_{H\alpha,\beta} = EW_{\text{cor}} \cdot F_{\lambda}$, where F_{λ} is the continuum flux density corresponding to the central wavelength of the $H\alpha$ or $H\beta$ line. We obtained this flux by using atmosphere models from Castelli & Kurucz (2003), which were scaled to the de-reddened G_{RP} flux of each star. Then, $L_{H\alpha,\beta} = 4\pi d^2 \cdot F_{H\alpha,\beta}$, where d is the distance to the sources. Following (Fairlamb et al. 2017, see also Mendigutía et al. 2011; Wichittanakom et al. 2020 and references therein) we can derive the accretion luminosity (L_{acc}) from the lines as:

$$\log(L_{\text{acc}}/L_{\odot}) = A + B \cdot \log(L_{H\alpha,\beta}/L_{\odot}), \quad (1)$$

where A and B are constants. For Herbig stars, Fairlamb et al. (2017) determined these constants to be $A = 2.09 \pm 0.06$ and $B = 1.00 \pm 0.05$ for the $H\alpha$ line and $A = 2.60 \pm 0.09$ and $B = 1.24 \pm 0.07$ for the $H\beta$ line.

Finally, the mass accretion rate (\dot{M}_{acc}) can be derived as:

$$\dot{M}_{\text{acc}} = \frac{L_{\text{acc}} R_{*}}{GM_{*}} = \frac{L_{\text{acc}}}{GM_{*}} \cdot \sqrt{\frac{L}{4\pi\sigma T_{\text{eff}}^4}}, \quad (2)$$

using the stellar parameters derived in Section 3. In case information about both the $H\alpha$ and $H\beta$ line is available, the derived accretion rates come from the $H\alpha$ line EW_{cor} (this was done for consistency, as stars with $H\alpha$ emission often have $H\beta$ in absorption). We derive accretion rates for 92 sources using the $H\alpha$ line and for 12 other sources using the $H\beta$ line. The mass accretion rates derived this way are tabulated in Table B3. We note that Equations (1) and (2) assume a magnetospheric accretion mechanism (Hartmann et al. 2016 and references therein).

6. PMS Nature of the Observed Sources

In this section, we assess the PMS nature of the observed sources by means of their location in the HR diagram, IR excesses, line profiles, and accretion rates. We note that it is beyond the capabilities of the data presented in this paper to assert with absolute certainty whether all the observed sources are indeed new Herbig discoveries. In fact, it is even proved difficult and controversial for much more intensely studied objects (e.g., HD 45677, Oudmajer & Miroshnichenko 2017). Nevertheless, in this section we provide ample and independent evidence to conclude that the vast majority, if not all, of the 137 considered sources (145–8, Section 4) are of a Herbig nature (see Appendix A for a description on the most dubious sources).

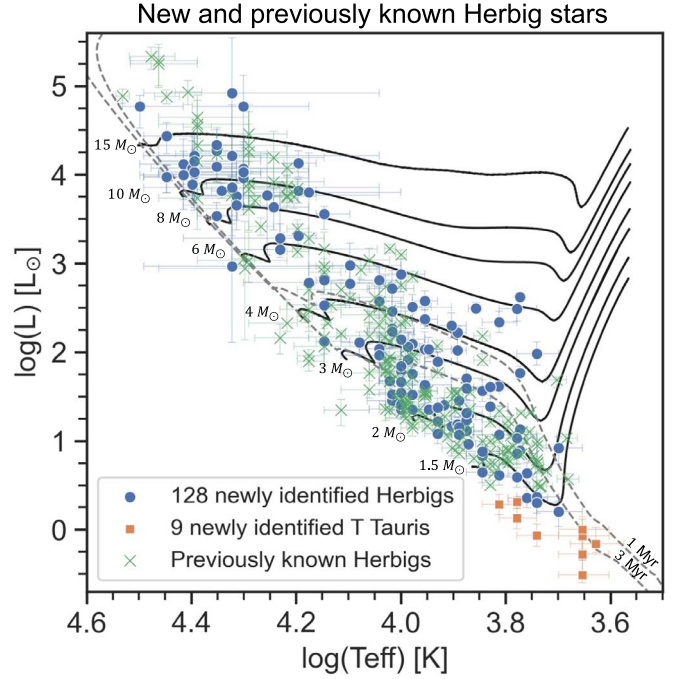


Figure 3. HR diagram of the 137 observed sources identified as PMS stars. Previously known Herbig Ae/Be stars and IMTTs with good astrometric quality are also shown. PARSEC 1.2S PMS tracks and isochrones corresponding to 1.5, 2, 3, 4, 6, 8, 10, 15 M_{\odot} and 1 and 3 Myr are presented (Bressan et al. 2012 and Marigo et al. 2017).

6.1. HR Diagram, Stellar Masses, and IR Excesses

In the HR diagram of Figure 3, it can be seen that most of the 137 observed sources are massive hot objects. In addition, none of the observed sources are located outside PMS locations in the HR diagram, although the proximity of some of them to the zero age main sequence (ZAMS) hampers a clear PMS identification. In the HR diagram of Figure 3 we also show previously known Herbig Ae/Be stars and IMTTs (from the compilations of Vioque et al. 2018; Guzmán-Díaz et al. 2021, and Valegård et al. 2021) with good astrometric solutions [$\sigma(\varpi)/\varpi \leq 1$, RUWE < 2 , and Fidelity > 0.95]. The stellar parameters of these previously known sources were rederived following Section 3 procedures to compare HR diagrams which are affected by the exact same systematics and uncertainties. We conclude that the observed sources are similarly distributed in the HR diagram to the previously known Herbig stars.

In Figure 4, we present the mass distribution of the 137 sources. In this figure, we also show the mass distribution of the previously known Herbig Ae/Be stars and IMTTs. We note that the observed sources and the previously known Herbig stars cover a similar mass range and have an analogous mass distribution. This is likely due to the fact that both groups are tracing the massive end of the IMF (see Vioque et al. 2018; Guzmán-Díaz et al. 2021). It is noteworthy that only three sources with $M > 15 M_{\odot}$ were observed, whereas there are several previously known Herbig stars over that mass. This is because PMS sources with those masses, in addition to being rare and often optically obscured, are typically at large distances and thus tend to have poor parallaxes. This caused those sources to be systematically excluded from the target selection of Section 2, which sampled the catalog of Herbig candidates of Vioque et al. (2020).

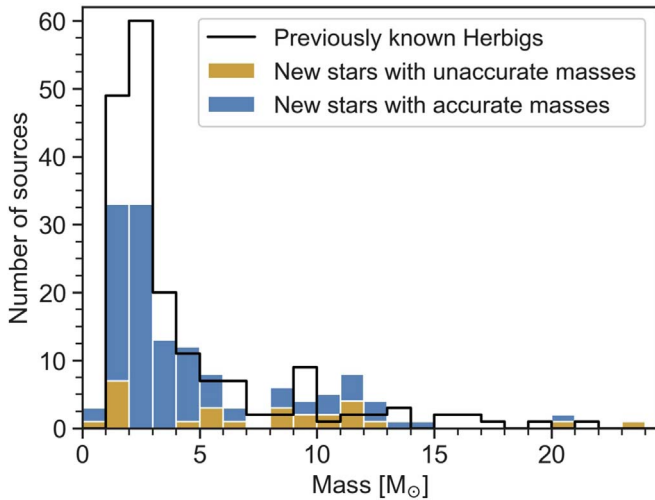


Figure 4. Histogram of the number of stars observed in this work per $1 M_{\odot}$ bin. In blue are the 110 observed stars with stellar mass determinations larger than three times the uncertainty [$M > 3\sigma(M)$]. In orange are the 27 stars with $M < 3\sigma(M)$. Contours trace the previously known Herbig Ae/Be stars and IMTTs with good astrometric quality.

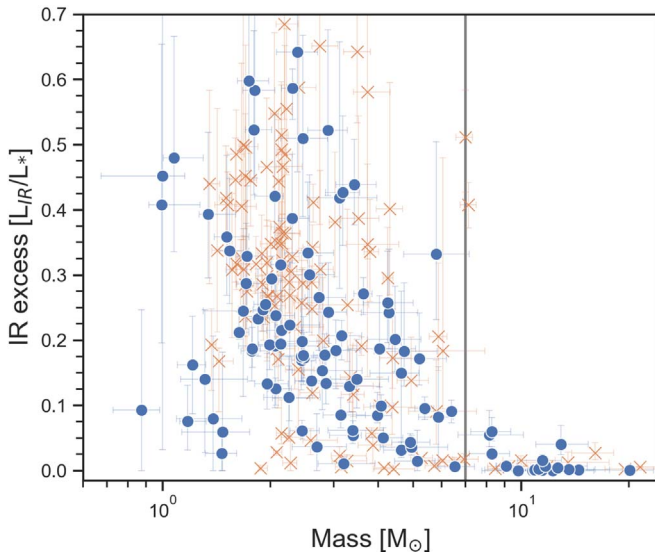


Figure 5. Mass vs. IR excess (L_{IR}/L_{*}). In blue are the stars observed in this work with $M > 3\sigma(M)$. Orange crosses show the IR excesses derived in Vioque et al. (2018) for the previously known Herbig stars with a good astrometric solution and $M > 3\sigma(M)$. The gray line traces the $7 M_{\odot}$ break in inner-disk dispersion efficacy.

In Figure 5, we plot the IR excesses derived in Section 3.2 for the observed sources as a function of mass. In this figure, we also show the values obtained for the previously known Herbig stars in Vioque et al. (2018). The observed sources have similar IR excesses to the previously known Herbig stars, and the break in inner-disk dispersion efficacy at $7 M_{\odot}$ discussed in Vioque et al. (2018) is also present for the observed objects.

6.2. Emission Lines and Accretion Rates

Regarding the presence of emission lines, 92 of the 100 sources with $H\alpha$ line observations show the line in emission. In addition, as discussed in Appendix A, of those eight sources without $H\alpha$ emission, seven show other emission lines. Of the 37 sources for which no $H\alpha$ line information is available 12

have emission in $H\beta$. We note that $H\beta$ emission may not be present even if $H\alpha$ emission is. This high percentage of sources with hydrogen emission supports the PMS nature of the group.

Regarding the $H\alpha$ line profiles, of the 92 stars with $H\alpha$ emission, 37 show single-peaked emission, 44 double-peaked emission, and 11 P-Cygni emission (of which five have inverse P-Cygni profiles). Therefore, 40% are single-peaked, 48% are double-peaked and 12% are P-Cygni. These percentages are similar to those observed for known Herbig stars (31%, 52%, and 17%, respectively; see Vioque et al. 2018). We suspect that the small difference between both groups is caused by the lower resolution of our observations, which moved many P-Cygni and double-peak profiles to the “single-peaked” group. We point out that similar percentages were found for the $\text{Br}\gamma$ line by Grant et al. (2022) in known Herbig stars.

The high fraction of double-peaked line profiles is also suggestive of the PMS nature of the observed sources; stellar activity would not necessarily result in double-peaked emission profiles and stellar winds would have resulted in a larger fraction of P-Cygni like shapes. The fraction of single-peaked $H\alpha$ profiles is consistent with the fraction of pole-on accretion disks that would be expected in a random distribution.

The accretion rates of this group of 92 sources with $H\alpha$ emission and 12 sources with $H\beta$ emission are presented in Figure 6 as a function of mass. In Figure 6, we compare these accretion rates with those obtained via the same procedure and assumptions in Wichittanakom et al. (2020) for a set of 163 previously known Herbig Ae/Be stars. The overlap between both sets in this parameter space is consistent with the observed sources being of a Herbig nature. This further supports that the $H\alpha$ and $H\beta$ emission used to derive the accretion rates is originated in a PMS accretion disk. There are, however, a few outliers in the trend of Figure 6. The accretion rates of the observed sources are analyzed in more detail in Section 7.

In this section, we have shown evidence for the Herbig nature of most of the observed sources. This can be summarized by their PMS location in the HR diagram (Figure 2), the amount of IR excess and its correlation with stellar mass (Figure 5), the presence of emission lines in their spectra, the shapes of the $H\alpha$ line, and the derived mass accretion rates (Figure 6). Therefore, of the 145 observed objects, we propose 128 sources to be new Herbig identifications, nine sources to be new massive T Tauri identifications (Section 3.3), and eight sources to be evolved stars of non-PMS nature (see Section 4). A closer look to the 128 proposed Herbig stars allowed us to determine 20 less secure identifications. These 20 stars are discussed in Appendix A.

7. Accretion Properties

The mass accretion rates derived in Section 5 from $H\alpha$ and $H\beta$ luminosities, together with the similar results of Wichittanakom et al. (2020), allow us to construct the largest sample of Herbig stars with mass accretion rate determinations to date. In total, we compile 258 Herbig sources with derived accretion rates between both works. We note that 48 of these sources have accretion rates that were derived in Fairlamb et al. (2015) by measuring the UV excess over the Balmer jump. This is a more direct measurement of the accretion rate, and it is free of the assumptions made when correlating accretion luminosity and emission line luminosities (see Mendigutía et al. 2015).

With this enhanced sample, we revisit the accretion rate properties of Herbig stars. In Figure 6, we show the accretion

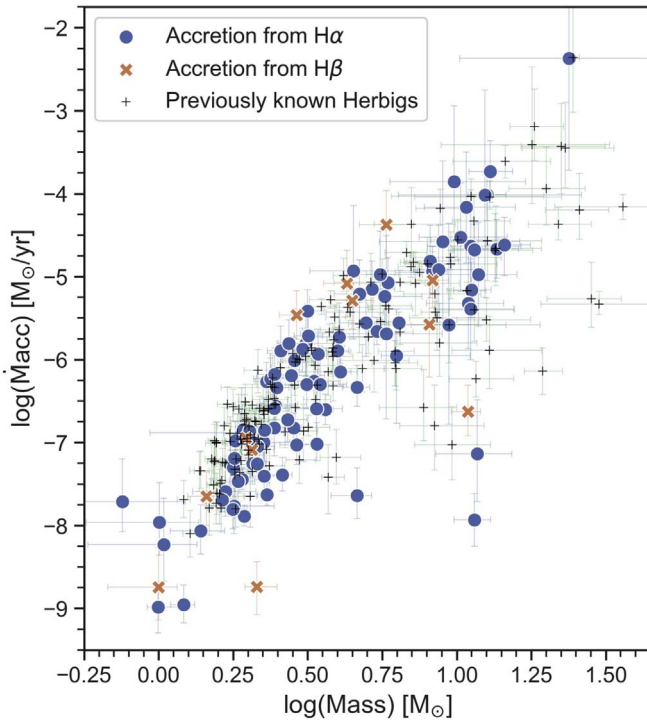


Figure 6. Mass vs. mass accretion rate. Blue filled circles indicate the 92 observed stars with accretion rates determined from $H\alpha$ measurements. Orange crosses indicate the 12 observed stars with accretion rates determined from $H\beta$ measurements. Black plus symbols trace the 163 previously known Herbig stars with mass accretion rates derived in Wichittanakom et al. (2020).

rate of this combined sample as a function of stellar mass. We note that for both new and previously known sources the mass accretion rate increases with stellar mass. As Wichittanakom et al. (2020) discussed, we also find that the accretion rate decreases with time during the PMS phase. However, it is not trivial to disentangle this effect from the dependence of the age on the mass.

In Wichittanakom et al. (2020) it was concluded that lower mass Herbig stars have a dependence of the mass on the accretion rate, characterized by a gradient that matches the gradient observed in the T Tauri regime (e.g., Calvet et al. 2004; Natta et al. 2006). However, higher mass Herbig stars show a smaller gradient in the mass vs. accretion rate relation. The break between both groups was set at $3.98_{-0.94}^{+1.37} M_{\odot}$. This accretion break and similar accretion gradients to those found in Wichittanakom et al. (2020) have also been identified by Grant et al. (2022), using a similar sample and the $Br\gamma$ line as the accretion tracer.

In a similar way to what was done in Section 5 of Wichittanakom et al. (2020), we looked for the mass value where the difference between the gradients of the low- and high-mass regimes maximizes. We note that this approach does not take into account the uncertainties in the accretion rate, nor the caveats of estimating the accretion rate from emission lines (see, e.g., Fairlamb et al. 2017; Mendigutía 2020). To study this difference between the observed gradients we use the S parameter. This parameter represents the significance of the difference of the slopes. It is defined as:

$$S = \frac{|b_1 - b_2|}{\sqrt{\sigma_{b_1}^2 + \sigma_{b_2}^2}}, \quad (3)$$

where b is the slope in each regime of the mass vs. accretion rate linear fit in log space, and σ^2 is the variance in that slope. The results of this study on the whole sample of 258 sources are illustrated in the top panels of Figure 7. In the top left panel, we show the S parameter as a function of the mass used to separate the low- from the high-mass regime. We calculated the S parameter for the sample of new Herbig stars, the sample of previously known Herbig stars, and the combination of those two samples. In all cases the S parameter increases with mass, up to a maximum at around $3\text{--}4 M_{\odot}$, and then monotonically decreases. Using a simple t -test approach, we conclude that the difference between gradients is significant to within 95% confidence if $S \gtrsim 2$. Hence, it is evident from Figure 7 that, within the Herbig regime, there is a change in the gradient of the accretion rate as a function of mass (see, however, Section 8.2 for a description of the caveats to consider when using line luminosities as accretion tracers).

The maximum S value found for all sources corresponds to a stellar mass for the break in gradient of $3.26 M_{\odot}$ (top right panel of Figure 7). This number is consistent with the value found in Wichittanakom et al. (2020) of $3.98_{-0.94}^{+1.37} M_{\odot}$. However, in the top right panel of Figure 7, it is noticeable that several sources are far from the general correlation. If we remove those “outliers” from the analysis (reducing the sample to 198 sources, bottom panels of Figure 7) we obtain a maximum S value at $3.87 M_{\odot}$, much closer to the central value of 3.98 derived in Wichittanakom et al. (2020).

Although there is a range of masses in which the gradient difference as traced by the S parameter is significant; there is a clear peak for S values in all samples at around $3\text{--}4 M_{\odot}$. This peak stands after removing the sources that deviate the most from the correlation. Thus, we confirm that the break in accretion rate detected in Wichittanakom et al. (2020) in the $3\text{--}4 M_{\odot}$ range holds with the sample of new Herbig stars. By using the maximum S values obtained for the different Herbig subsamples, we further constrain the potential break in accretion rate to a mass of $3.87_{-0.96}^{+0.38} M_{\odot}$ (corresponding to the mass of a B7–B8 MS star).

8. Discussion

In the previous sections, we present and discuss 128 new Herbig stars homogeneously selected and observed, for which we provide accurate stellar parameters. In this section, we put these sources in context with the historically considered Herbig stars, and explain why these new Herbig stars provide interesting insights to the intermediate- to high-mass star formation scenario.

8.1. General Remarks

Among the main caveats of previous studies dedicated to intermediate- to high-mass PMS stars is the low number of sources in any given mass or age range (e.g., Vioque et al. 2018; Guzmán-Díaz et al. 2021; van der Marel & Mulders 2021). The sample of 128 new Herbig stars contains both low-mass objects at the boundary with the T Tauri regime and very-massive PMS objects (see Figures 3 and 4). In the mass range of $1.5\text{--}4 M_{\odot}$ we present 73 new sources increasing by 42% the number of known objects. In the mass range of $4\text{--}8 M_{\odot}$ we present 23 new sources, increasing by 70% the number

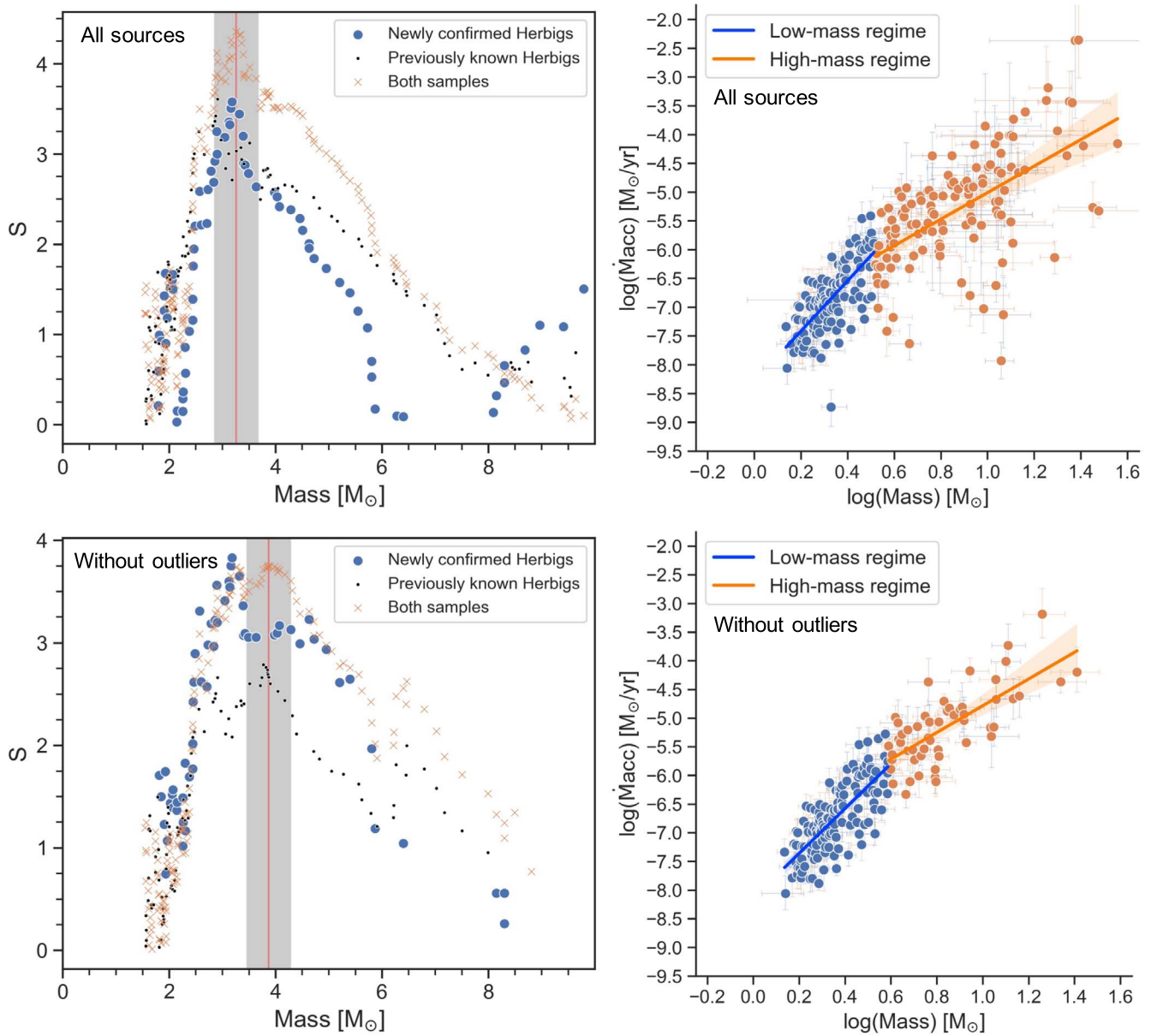


Figure 7. Left plots: stellar mass used to separate the low-mass regime from the high-mass regime as a function of the S parameter. Red line traces the maximum S value when all sources are considered, with its estimated uncertainty (gray shaded region). Right plots: mass vs. mass accretion rate for the low- and high-mass regimes, which were defined by the maximum S value obtained in the plots on the left. The fits that gave the gradients with the maximum S value are shown, with a 95% confidence interval.

of known objects (55 sources are above the $4 M_{\odot}$ threshold of Wichittanakom et al. 2020 for the break in accretion properties). In the mass range of PMS stars above $7\text{--}8 M_{\odot}$ (typically considered the MYSO regime) we present 32 new sources, increasing by 80% the number of known objects. This is the threshold of Vioque et al. (2018) from which very effective inner-disk-dispersal mechanisms are acting. These statistics, summarized in Table 2, use as reference the sample of historically known Herbig stars considered in Vioque et al. (2018), Guzmán-Díaz et al. (2021), and Vægård et al. (2021) with mass determinations. However, other less famous objects of the class do exist in the literature, like the recently proposed 58 Herbig Ae/Be sources from the LAMOST survey (Shridharan et al. 2021; Zhang et al. 2022), the 13 proposed Herbig Ae/Be stars in the Small Magellanic Cloud (Keller et al. 2019), or the 77 IMTTs found in the Carina Nebula (Nuñez et al. 2021).

The most massive of the newly discovered Herbig stars appear to overlap with the class of Massive Young Stellar Objects (Frost et al. 2021; Koumpia et al. 2021). More than 300 such objects with luminosities larger than $5000 L_{\odot}$, corresponding to masses larger than around $8\text{--}10 M_{\odot}$, are listed as MYSO in the RMS catalog (Lumsden et al. 2013). These massive young stars are infrared bright due to the large amounts of dusty material obscuring them from sight and, as a result, they were historically assumed to be optically invisible. Intriguingly, however, some were already reported to be visible in the optical. For example, the objects PDS 27 and PDS 37 appear in the RMS catalog (see also Koumpia et al. 2019), but with V band magnitudes of ~ 13 mag they are optically bright enough to have been recognized as Herbig Be stars (Ababakr et al. 2015; Vioque et al. 2018). Given that Gaia, with its faint magnitude limit of ~ 20 mag, pushes the definition of optically

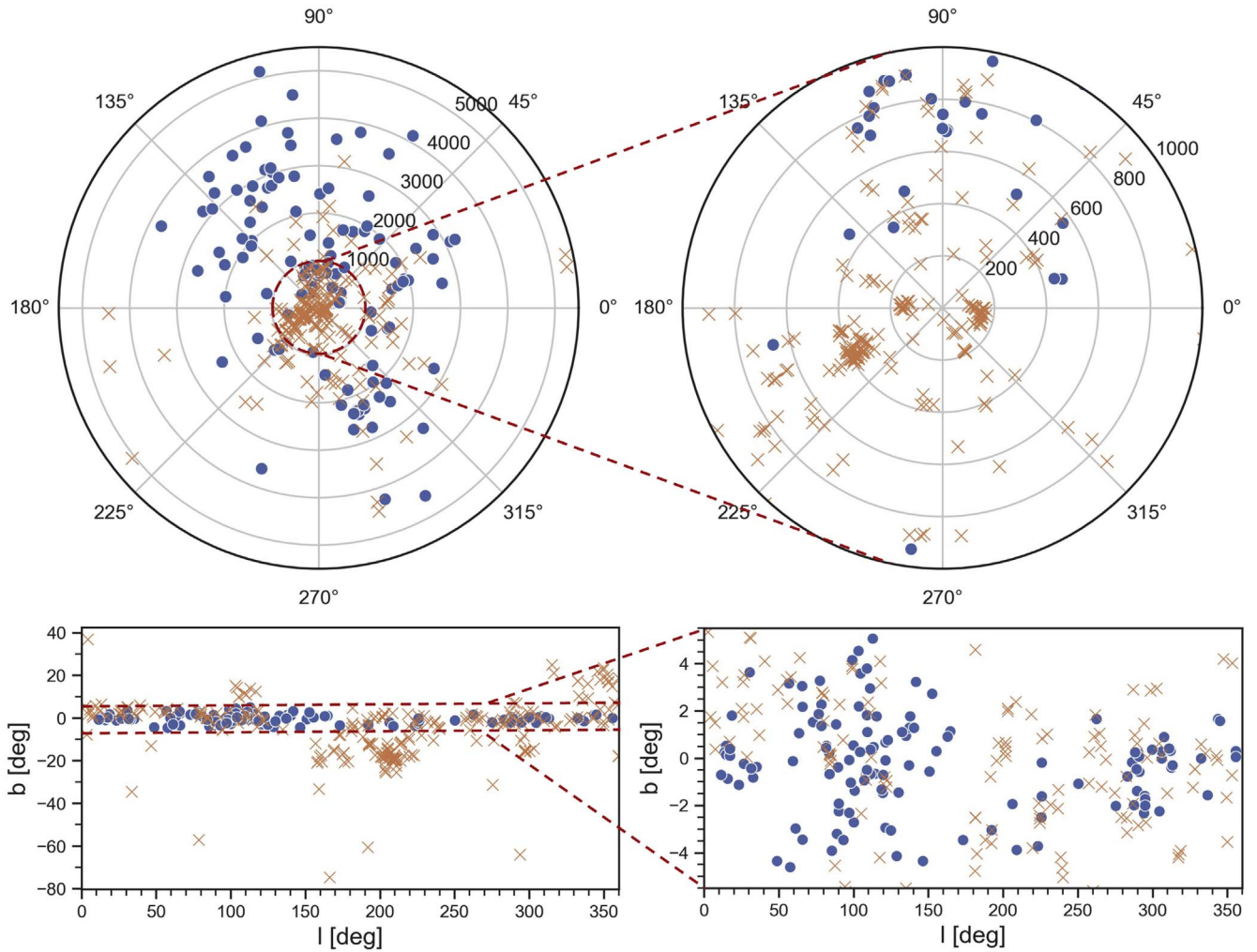


Figure 8. The 128 newly confirmed Herbig stars are presented as blue dots. Orange crosses trace all 232 previously known Herbig stars in the literature with Gaia EDR3 parallaxes (ϖ) and $\sigma(\varpi)/\varpi < 1$. Panels on the right are a close up look at the panels on the left. Top left: Galactic longitude vs. distance, each circular grid line is 1 kpc, up to 5.5 kpc. Top right: Galactic longitude vs. distance, each circular grid line is 200 pc, up to 1000 pc. Bottom left: Galactic longitude vs. Galactic latitude. Bottom right: Galactic longitude vs. Galactic latitude limited to $-5.5 < b < 5.5$ deg, where the newly identified stars are confined.

Table 2
Number of known Herbig Stars Per Stellar Mass Range

Mass Range (M_{\odot})	Previously Known	This work	Increase
1.5–4	173	73	42%
4–8	33	23	70%
>8	40	32	80%
Total	246	128	

Notes. For the previously known objects, we only consider the sources discussed in Vioque et al. (2018), Guzmán-Díaz et al. (2021), and Valegård et al. (2021) with mass determinations.

visible to much fainter magnitudes, the new Gaia-discovered Herbig stars may well bridge the gap between the (optically bright) Herbig Be stars and the optically faint MYSOs. The fact that this project already adds 32 new sources to this mass regime evidences this hypothesis, while preliminary reports show that around 20% of the previously optically undetected MYSOs may have a Gaia counterpart (R. Shenton et al. 2022,

private communication). Clearly, Gaia plays an important role regarding the most massive young stellar objects.

Regarding the age of the sources, the sample of 128 new Herbig stars contains both sources close to the ZAMS and at earlier stages of evolution. Although some stars could be considered IMTTs (see, e.g., Valegård et al. 2021), most sources clearly belong to the Herbig Ae/Be regime (see Section 1 and footnote 1). With the exception of the four sources discussed in Appendix A, the age range covered at every mass bin is equivalent to the age range covered by previously known and analyzed objects. Given that the Vioque et al. (2020) catalog is HR-diagram independent, this is probably not caused by a selection bias but by the fact that younger objects are too embedded to appear in the Gaia survey.

There are some biases in the catalog of Vioque et al. (2020) that affect the sample of 128 new Herbig stars. These are mainly that sources with strong IR excesses and H α emission were favored in the selection. This biases the sample toward the more “active” PMS objects. We refer the reader to Vioque et al. (2020) for more details.

In Figure 8 we plot the distances and galactic coordinates of the 128 new Herbig detections. To these we add all previously known Herbig stars (Table 2) with Gaia EDR3 parallaxes and

$\sigma(\varpi)/\varpi < 1$. The new Herbig stars are confined to the Galactic plane because of selection effects in Vioque et al. (2020). They are generally fainter than the previously known Herbig stars (see Table B1), and hence they are typically further away. There are only five new Herbig stars within 500 pc, 80% of the new sources being beyond 1 kpc.

8.2. Interpretation of the Change in Accretion Gradient

In this section, we interpret the break in accretion gradient at 3–4 M_{\odot} identified in Wichittanakom et al. (2020) and Grant et al. (2022), that we extend to the new Herbig stars in Section 7 and constrain to $3.87^{+0.38}_{-0.96} M_{\odot}$. The most accepted interpretation for this change in accretion gradient is that low-mass objects are subjected to magnetospheric accretion (see Bouvier et al. 2007), whereas a fraction of the more massive objects are accreting through a different mechanism; possibly the boundary-layer accretion mechanism (Mendigutía 2020).

We should caution, however, that the accretion rates derived in Section 5 assume a magnetospheric accretion scenario. If a different accretion mechanism applies for some objects their derived accretion rates might be highly inaccurate (see Section 6 of Wichittanakom et al. 2020). For example, if a boundary-layer accretion mechanism (Mendigutía 2020) is applying for sources more massive than 3–4 M_{\odot} , the accretion luminosity to accretion rate relation of Equation (2) would need to be corrected by the relative difference in rotational velocities between the star and the gas contact phase (see Section 1.3 of Wisniewski et al. 2021 for more details). In addition, the relation between the line luminosities and the accretion luminosity (Equation (1)) would have to be revisited for the boundary-layer scenario. Therefore, we advise the reader to treat the accretion rates derived in this work for massive stars with caution.

In addition, there are alternative explanations to the change of trend in hydrogen line luminosity properties, apart from a change in accretion mode (see Mendigutía et al. 2015; Marcos-Arenal et al. 2021). For example, outflowing material could be dominating the line emission (caused by, e.g., disk photo-evaporation, Guzmán-Díaz et al. 2021). Indeed, it is not straightforward to characterize the origin of the hydrogen emission lines in high-mass Herbig stars (Mendigutía et al. 2017; Mendigutía 2020, and references therein). This contrasts to what we observe for the lower mass objects, where the hydrogen emission lines seem to originate in the magnetosphere (Bouvier et al. 2020; Gravity Collaboration et al. 2020).

Furthermore, there is an observational bias to consider. High-mass PMS stars are optically visible for a much shorter time than low-mass PMS stars, and they are often heavily obscured, especially at the younger ages. Hence, in our optical analysis we might be biased against the strongest accretors in the high-mass regime.

Because of the reasons stated in this section, it is not straightforward to deduce a break in accretion properties only from the break in the behavior of the hydrogen lines. However, this break at 3–4 M_{\odot} has been independently detected using different techniques (e.g., near-IR interferometry, Monnier et al. 2005; optical- and near-UV spectropolarimetry, Ababakr et al. 2017; spectro-photometry, Mendigutía et al. 2011; Fairlamb et al. 2015). It is the combination of those results together with the accretion rates derived from emission lines that lead us to conclude that the break in accretion properties of Figure 7 is likely due to a change between accretion

mechanisms; from magnetospheric accretion applying to the lower mass objects to a boundary-layer-like accretion mechanism acting in some, or most, of the more massive objects.

8.3. Evaluation of Vioque et al. (2020) Results

The target list of the observations presented in this work was extracted from the catalog of new intermediate- to high-mass PMS candidates of Vioque et al. (2020). In this section, we reevaluate the accuracy and quality of that catalog.

In the Vioque et al. (2020) catalog, 2226 new Herbig candidates were presented (with $\sigma(\varpi)/\varpi \leq 0.2$, this number remains similar when the astrometry is updated to EDR3). We note that, although the catalog is astrometry independent, arbitrary cuts to the astrometric quality are necessary to select massive objects with a certain degree of confidence. In this work we have observed 145 objects, which is roughly 6% of the whole catalog. As mentioned in Section 2, the target selection was based only on the absolute magnitude and on the parallax quality of the sources. Hence, the target list is representative of the whole catalog of new intermediate- to high-mass PMS stars of Vioque et al. (2020).

The number of contaminants we have found in this work (8/145 or 5.5%) is consistent with the estimated lower-limit precision of the Vioque et al. (2020) catalog ($P \gtrsim 81\%$). This affirmation holds true even when we consider as contaminants the more dubious sources of Appendix A (28/145 or 19%). We note that the Vioque et al. (2020) catalog is HR diagram independent and thus the high proportion of massive stars targeted (134/145 sources, 92%, are above 1.5 M_{\odot} , see Section 3.3) is a compelling positive assessment of that catalog. Therefore, we conclude that the observations presented in this work give independent support to the quality and robustness of the Vioque et al. (2020) catalog.

In addition, 14 classical Be candidates from the Vioque et al. (2020) catalog were observed (these are non-PMS stars which are typical contaminants in Herbig samples, see Vioque 2020). None of these Classical Be candidates could be identified as a misclassification (e.g., by showing a PMS nature). The discussion on the observations of these sources will be presented in an independent paper.

Because of sensitivity limitations, mostly candidates at the bright end of the Vioque et al. (2020) catalog were observed (90% of the observed sources are in the $12 < G < 14$ mag range). One could therefore argue that the observed sample is biased. However, the Vioque et al. (2020) catalog is distance independent. Hence, the conclusions that arise from these observations can be extrapolated to the fainter objects of the catalog, given that they were all selected homogeneously by the machine-learning algorithm.

9. Conclusions

In this work, we discuss the results of the spectroscopic observations of a sample of 145 Herbig candidates from the catalog of Vioque et al. (2020). The main results and conclusions of these observations are the following:

1. We propose 128 sources as new “Herbig” identifications (i.e., PMS stars with $M > 1.5 M_{\odot}$). We provide ample evidence supporting this classification. This evidence is based on their PMS location in the HR diagram, the amount of IR excess and its correlation with stellar mass, the presence of emission lines in their spectra, the shapes

of the $H\alpha$ line, and the derived mass accretion rates. Only five sources lie within 500 pc, whereas 75% of the stars are between 1 and 4 kpc. Twenty sources were flagged as less secure identifications.

2. We derive extinctions and accurate stellar parameters for all sources, placing them in the HR diagram by means of Gaia EDR3 parallaxes.
3. This sample of 128 new Herbig stars increases the number of known objects of the class by $\sim 50\%$. The sources are distributed over a representative range in mass and age when compared to previously known Herbig stars. According to classical definitions, most of the observed sources fall within the Herbig Ae/Be or the Massive Young Stellar Objects regime, but some stars can be considered Intermediate-Mass T Tauris. In particular, 23 of the new sources have masses between $4\text{--}8 M_{\odot}$ and 32 sources have masses $>8 M_{\odot}$.
4. Four sources were identified as new “unclassified B[e]” (FS CMa) discoveries. Nine other sources were also identified as having a PMS nature, but their masses assign them to the T Tauri regime.
5. We derive accretion rates for 104 of the new Herbig stars by using hydrogen emission lines ($H\alpha$ and $H\beta$ luminosities). This is a 60% increment to the number of Herbig stars with derived accretion rates. The change in accretion gradient as a function of mass in the $3\text{--}4 M_{\odot}$ range described in Wichittanakom et al. (2020) is also present for the new Herbig stars. This provides further support to a change in accretion mechanism happening within the Herbig regime. We constrain the mass for this possible change to $3.87_{-0.96}^{+0.38} M_{\odot}$ (the mass of a B7–B8 main-sequence star).
6. There are four sources (VOS 63, VOS 67, VOS 821, and VOS 1635) of $5\text{--}6 M_{\odot}$ which are younger than previously known PMS stars of that mass.
7. The sudden decrease in the amount of near- and mid-IR excess at $\sim 7 M_{\odot}$ described in Vioque et al. (2018) for the historically considered Herbig stars is also present for the new sources. For this group of Herbig stars, $M > 7 M_{\odot}$ corresponds to sources with $T_{\text{eff}} \gtrsim 15,000$ K. This further supports the idea of very effective inner-disk dispersion mechanisms acting on massive stars, like the disk photoevaporation mechanism proposed in Guzmán-Díaz et al. (2021).
8. The observations described in this work provide independent support to the accuracy and high quality of the catalog of new intermediate- to high-mass PMS stars presented in Vioque et al. (2020), of which these observations constitute a mere 6%.

These observations yield a well-defined set of new intermediate- to high-mass PMS stars. Contrary to previous samples, these new Herbig stars were homogeneously identified and observed. Therefore, this set of objects will be the basis for future surveys and follow-up observations dedicated to the Herbig group and their protoplanetary disks. The sample of new Herbig stars presented in this work will be complemented by an X-Shooter Very Large Telescope survey focusing on newly identified Intermediate-Mass T Tauri stars (D. Iglesias et al. 2022, in preparation). All together, the two surveys will increase by a factor of two the number of known intermediate- to high-mass PMS objects, covering

representatively all the stages of the optical evolution of massive forming stars.

The STARRY project has received funding from the European Union’s Horizon 2020 research and innovation program under MSCA ITN-EID grant agreement No 676036. Ignacio Mendigutía is funded by a RyC2019-026992-I grant by MCIN/AEI /10.13039/501100011033. This work has made use of data from the European Space Agency (ESA) mission Gaia (<https://www.cosmos.esa.int/gaia>), processed by the Gaia Data Processing and Analysis Consortium (DPAC, <https://www.cosmos.esa.int/web/gaia/dpac/consortium>). Funding for the DPAC has been provided by national institutions, in particular the institutions participating in the Gaia Multilateral Agreement. This research has made use of IRAF which is distributed by the National Optical Astronomy Observatory, which is operated by the Association of Universities for Research in Astronomy (AURA) under a cooperative agreement with the National Science Foundation. This research has made use of the TOPCAT tool (Taylor 2005). In addition, this research used the VizieR catalog access tool, and the SIMBAD database developed and operated at CDS, Strasbourg, France.

This article is based on observations made in the Observatorios de Canarias del IAC with the Isaac Newton Telescope (INT) operated on the island of La Palma by the Isaac Newton Group of Telescopes in the Observatorio del Roque de los Muchachos. In addition, this article is based on observations collected at the Centro Astronómico Hispano-Alemán (CAHA) at Calar Alto, operated jointly by Junta de Andalucía and Consejo Superior de Investigaciones Científicas (IAA-CSIC). Finally, this article also used observations collected at the European Organisation for Astronomical Research in the Southern Hemisphere under ESO programmes 0104.C-0937(A) and 0104.C-0937(B).

Appendix A Less Secure Identifications

Among the 128 new Herbig stars proposed, there are 20 sources which, for different reasons, have a less secure PMS nature than the rest. These sources are discussed in detail in this appendix.

Eight sources have $H\alpha$ and $H\beta$ fully in absorption (VOS 209, VOS 448, VOS 491, VOS 495, VOS 668, VOS 854, VOS 1922, and VOS 2060). However, three of these sources (VOS 448, VOS 495, and VOS 1922) show an asymmetric $H\alpha$ absorption profile, which might hint at some $H\alpha$ emission. These eight sources are shown in the HR diagram of Figure 2. Although emission in hydrogen lines is historically one of the defining properties of Herbig stars, some intermediate-mass PMS stars lack hydrogen emission. Hence, this fact alone is inconclusive for removing these sources from the PMS category. In addition, of the eight sources for which we do not detect clear hydrogen emission, seven show other emission lines (the exception is VOS 854). However, VOS 448, VOS 495, VOS 1922, and VOS 2060 do not show any significant level of IR excess, and the IR excess of VOS 491 is clearly spurious (see Section 3.2). Because hydrogen emission lines and IR excess are the main indicators of YSO nature, we label these latter five sources plus VOS 854 as less secure identifications. We note that 37 observed sources lack $H\alpha$ information, and hence the aforementioned analysis could not

be applied to them. Of these, seven sources have $H\beta$ in absorption and display little IR excess ($L_{\text{IR}}/L_* < 0.03$). These are VOS 821, VOS 879, VOS 1225, VOS 1276, VOS 1771, VOS 1913, and VOS 2051, which are also labeled as less secure identifications.

We now consider the nature of VOS 209 and VOS 668, which have emission lines and IR excess but lack hydrogen emission. van den Ancker et al. (2021) found that the intermediate-mass YSO HD 152384 has all hydrogen lines strictly in absorption, but has refractory lines in emission. This led van den Ancker et al. (2021) to suggest that HD 152384 is at the late stages of the PMS phase and is surrounded by a tenuous circumstellar disk caused by the collision of rocky planets (see also the extreme debris disks described in Moór et al. 2021). We pose VOS 209 and VOS 668 as PMS sources of a similar nature to HD 152384. Indeed, the age estimates derived in Section 3.3 imply that both VOS 209 and VOS 668 are compatible with being close to the main sequence ($7.27^{+0.10}_{-0.19}$ and $6.61^{+0.16}_{-0.09}$ Myr, respectively). These two sources are marked in Figure 2.

In addition, we found four sources (VOS 1405, VOS 1440, VOS 2158, and VOS 2161) that have so many permitted and forbidden emission lines that the underlying photospheric absorption spectrum is hardly visible. They are reminiscent of the “unclassified B[e]” objects (Lamers et al. 1998), which constitute a class that includes both evolved stars and young Herbig stars. However, it is often hard to decide on the evolutionary nature of the objects. For example, the archetypal unclassified B[e] star HD 45677 may or may not be a young star (see Oudmaijer & Miroshnichenko 2017; Hofmann et al. 2022). Such sources are also referred to as FS CMa objects

(Miroshnichenko 2007). We therefore propose VOS 1405, VOS 1440, VOS 2158, and VOS 2161 to be new “unclassified B[e]” (FS CMa) discoveries. The absence of clear photospheric hydrogen absorption lines combined with multiple emission lines led to this FS CMa classification. The nature of these sources is unclear, but they could still be of a YSO nature. These new “unclassified B[e]” discoveries are highlighted in the HR diagram of Figure 2.

Finally, there are four sources (VOS 63, VOS 67, VOS 821, and VOS 1635), which are younger than all previously known Herbig stars of a similar mass ($5\text{--}6 M_{\odot}$, see Figure 3). PMS objects of this high mass and young age are expected to be quite embedded. Thus, these sources require a closer look at their nature. VOS 821 was already mentioned in this appendix regarding its lack of observed hydrogen emission and IR excess. However, we do not have any reason to suspect of the PMS nature of the other three objects, although a post-MS nature can neither be entirely discarded. It has been proposed that the FU Ori outbursting phenomena, which can cause T Tauri stars to get bluer and more luminous (e.g., Vorobyov et al. 2017; Kuffmeier et al. 2018), might explain the position of PMS sources in this region of the HR diagram. However, should that be the case we would expect to measure large $H\alpha$ EWs signposting high accretion rates, and that is not the case for these sources.

The 20 sources discussed in this appendix are flagged in Tables B2 and B3.

Appendix B Tables

This appendix contains Tables B1, B2, and B3.

Table B1
Log of Observations

Name	Gaia EDR3 source id	Alternative name	R.A. hh:mm:ss	Decl. dd:mm:ss.s	Obs Date		Exposure Time		Spectrograph	G_{BP} [mag]	G [mag]	G_{RP} [mag]
					Blue	Red	Blue [s]	Red [s]				
VOS 4	5524619735681532160		08:51:11.43	-41:38:49.9	2020-03-12	2020-03-20	900	1100	EFOSC2	13.45	13.20	12.64
VOS 7	2013474586693428096		22:54:03.79	+58:54:01.5	2019-09-04		450		CAFOS	13.59	12.82	12.22
VOS 15	4054609866596686336	V731 Sco	17:33:20.78	-32:34:25.7	2020-03-13	2020-03-20	1000	2000	EFOSC2	14.02	13.62	12.99
VOS 20	2206875422143048960		22:50:57.07	+61:23:37.7	2019-08-06	2019-08-12	1000	1800	IDS	14.99	14.22	13.37
VOS 22	2164505844663760768		21:11:19.06	+47:38:47.6	2019-08-06	2019-08-10	600	900	IDS	12.68	12.30	11.68
VOS 24	4267078153499687296	V868 Aql	18:56:47.65	+01:48:51.2	2019-08-06	2019-08-11	750	1300	IDS	14.00	13.15	12.22
VOS 26	5337719389118815488	ES Car	11:10:13.23	-60:14:03.4	2020-03-12	2020-03-20	1000	1600	EFOSC2	13.56	13.19	12.70
VOS 32	425559107889037568	FY Cas	00:38:50.08	+59:54:10.0	2019-08-06	2019-08-12	1200	1500	IDS	15.60	14.58	13.56
VOS 35	2208975695512792064		23:10:11.33	+65:55:58.9	2019-09-04; 05		900; 900; 900		CAFOS	14.00	13.29	12.37
VOS 42	2016307791941936896	GGR 156	23:42:26.73	+63:37:38.7	2019-08-07	2019-08-10	900	1200	IDS	14.00	13.10	12.14
VOS 48	2204517656901678848		22:11:42.82	+60:36:43.3	2019-08-05	2019-08-09	1000	2100	IDS	14.77	14.01	13.09
VOS 50	3348898739291597568		06:01:53.76	+16:22:36.6	2020-03-12		1200		EFOSC2	16.22	15.41	14.49
VOS 51	2067030702869079424	LkHA 371	20:47:23.59	+43:44:39.7	2019-08-05	2019-08-09	300	900	IDS	12.72	12.28	11.73
VOS 55	5312087505304128000		09:26:45.84	-53:32:46.8	2020-03-12	2020-03-19	1500	2200	EFOSC2	14.40	13.78	13.03
VOS 56	2208194286334441344	BW Cep	22:41:16.98	+63:02:37.9	2019-08-07	2019-08-11	900	1200	IDS	13.67	13.71	12.36
VOS 63	1836558703328498944		20:10:27.24	+27:05:27.7	2019-08-06	2019-08-10	750	1200	IDS	14.89	13.53	12.40
VOS 67	2031912537697905536	V989 Cyg	19:48:38.56	+30:02:41.4	2019-08-06	2019-08-11	600	1300	IDS	13.37	12.41	11.44
VOS 69	2166981120209304576	V522 Cyg	20:59:05.92	+48:05:36.8	2019-08-08	2019-08-11	600	1000	IDS	14.32	13.88	12.91
VOS 70	430854252809011200	[KW97] 3-17	00:36:51.77	+63:29:30.1	2019-08-05	2019-08-09	600	900	IDS	13.96	12.91	11.84
VOS 76	5337981412138546432		10:56:32.82	-61:14:08.7	2020-03-12	2020-03-21	1000	1400	EFOSC2	13.68	13.24	12.57
VOS 77	430707601141581952	GGR 195	00:37:22.54	+62:44:27.3	2019-09-05		600; 600		CAFOS	13.29	12.66	11.90
VOS 78	4145745975926657664		18:15:28.31	-15:51:03.0	2019-08-07	2019-08-11	900	900	IDS	14.25	13.83	13.21
VOS 84	201374425057424512		05:08:13.05	+42:14:55.8	2019-09-04		800		CAFOS	13.69	13.34	12.77
VOS 95	5940955031917319040		16:41:18.87	-48:44:31.1	2020-03-12	2020-03-19	600	1800	EFOSC2	13.09	12.74	12.18
VOS 104	2027980718477508480	IZ Vul	19:47:16.49	+27:19:55.7	2019-08-08	2019-08-12	600	1000	IDS	13.20	12.79	12.18
VOS 105	2020080113265080832		19:42:28.11	+23:06:51.4	2019-08-05	2019-08-10	900	1000	IDS	15.35	14.43	13.47
VOS 108	5350683490177538944		10:37:00.18	-58:35:33.8	2020-03-13	2020-03-20	600	1200	EFOSC2	13.59	13.33	12.83
VOS 111	2066439165609688192		20:39:12.72	+42:20:54.6	2019-08-07	2019-08-12	1000	1500	IDS	15.35	14.37	13.35
VOS 112	5868455988315314560		13:30:00.32	-61:37:33.9	2020-03-12	2020-03-21	1200	1200	EFOSC2	14.71	13.78	12.76
VOS 118	1971703422709930496		21:20:36.31	+45:14:41.1	2019-09-05		1200; 800		CAFOS	14.22	13.68	12.99
VOS 121	2178435351312223488	V488 Cep	21:35:19.16	+57:36:38.1	2019-08-07	2019-08-11	900	900	IDS	13.55	13.19	12.63
VOS 125	4256500851683628544	THA 14-26	18:40:55.76	-05:34:38.1	2019-08-05	2019-08-11	750	1500	IDS	14.03	13.33	12.48
VOS 131	3349361015210583168	V339 Ori	06:01:04.65	+16:54:40.6	2020-03-12	2020-03-19	250	1400	EFOSC2	13.04	12.53	11.84
VOS 135	2032083584842678144	V1352 Cyg	19:44:29.75	+30:14:50.2	2019-08-06	2019-08-10	750	1200	IDS	14.64	14.06	13.33
VOS 136	4097464668003385216		18:14:06.54	-17:02:58.6	2020-03-14	2020-03-21	1200	1200	EFOSC2	13.64	12.92	12.06
VOS 140	428909457258627200		00:22:42.11	+61:12:23.3	2019-08-05	2019-08-09	1200	1200	IDS	15.17	14.89	14.40
VOS 164	4315228344710978816		19:36:22.23	+11:52:44.1	2019-08-08	2019-08-09	900	900	IDS	14.11	13.86	13.46
VOS 184	2015682857022899840		23:27:57.76	+61:46:07.6	2019-08-06	2019-08-12	1000	2100	IDS	15.34	14.82	14.11
VOS 199	1823174039068377216	DW Sge	19:55:54.29	+19:32:35.4	2019-09-03		800		CAFOS	13.35	13.09	12.63
VOS 200	250764453016220800		04:05:49.37	+51:28:34.5	2019-09-04		800		CAFOS	13.66	12.93	12.06
VOS 209	5941445658948980864		16:23:39.76	-49:12:09.9	2020-03-12	2020-03-20	800	1600	EFOSC2	13.78	13.38	12.80
VOS 215	5969536355649568640		16:52:53.75	-41:22:09.2	2020-03-13	2020-03-20	800	1600	EFOSC2	13.60	13.34	12.91
VOS 224	5866510505529424896		14:14:18.14	-61:41:54.0	2020-03-12	2020-03-19	500	1000	EFOSC2	13.34	13.08	12.65
VOS 233	5337668772877422464		11:10:39.18	-60:23:52.8	2020-03-13	2020-03-20	700	1400	EFOSC2	13.66	13.36	12.87
VOS 247	1969788039090648832		21:10:36.95	+42:20:57.0	2019-08-08	2019-08-11	600	1000	IDS	13.76	13.42	12.89
VOS 250	2062526622213061760	[OH83] B343 S3	20:14:08.98	+40:29:50.2	2019-09-03		600		CAFOS	13.04	12.77	12.30
VOS 253	3049153761980978560		06:57:11.43	-10:57:29.0	2020-03-13	2020-03-19	600	1300	EFOSC2	13.24	13.05	12.74

Table B1
(Continued)

Name	Gaia EDR3 source id	Alternative name	R.A. hh:mm:ss	Decl. dd:mm:ss.s	Obs Date		Exposure Time		Spectrograph	G_{BP} [mag]	G [mag]	G_{RP} [mag]
					Blue	Red	Blue [s]	Red [s]				
VOS 271	465485914143803136		02:34:10.27	+61:24:40.4	2019-09-05		1200		CAFOS	14.42	13.85	13.10
VOS 274	2207681742123365120		23:02:28.52	+63:16:31.0	2019-09-04		550		CAFOS	13.47	13.03	12.40
VOS 284	4054618520934162944	V486 Sco	17:34:37.86	-32:36:18.6	2020-03-14	2020-03-20	750	1000	EFOSC2	12.81	12.45	11.91
VOS 290	5333514409950744704	WRAY 15-821	11:31:13.38	-63:50:12.0	2020-03-12	2020-03-19	900	1600	EFOSC2	13.42	12.88	12.10
VOS 293	5333596770242078976	ESO-HA 303	11:36:19.60	-63:15:06.3	2020-03-12	2020-03-21	900	1200	EFOSC2	13.36	13.20	12.89
VOS 297	2059037012843484032	V1476 Cyg	20:08:44.81	+35:40:31.2	2019-09-03		900		CAFOS	14.09	13.56	12.80
VOS 321	2068318948239115008		20:21:36.07	+40:47:56.2	2019-09-05		800		CAFOS	12.86	12.58	12.12
VOS 336	1972408072220900864		21:22:05.93	+46:51:40.6	2019-09-04		800; 800		CAFOS	13.56	12.84	12.01
VOS 341	5333575329766038144	ESO-HA 306	11:39:56.77	-63:29:26.6	2020-03-13	2020-03-21	900	1600	EFOSC2	14.12	13.89	13.48
VOS 361	3044960396431590784		07:05:47.24	-12:23:48.8	2020-03-12	2020-03-19	1000	2000	EFOSC2	13.03	12.73	12.24
VOS 373	3131337377071123200		06:32:24.56	+04:59:37.8	2020-03-14	2020-03-19	600	1200	EFOSC2	12.75	12.38	11.82
VOS 398	2067485110409323648		20:25:38.84	+40:19:00.8	2019-09-03		900; 434		CAFOS	13.96	13.50	12.88
VOS 406	5328760495308550400	Ve 6-19	08:54:12.39	-47:37:21.4	2020-03-12	2020-03-20	1200	1600	EFOSC2	13.67	13.00	12.18
VOS 413	5337250722275063936		11:10:46.64	-61:06:25.6	2020-03-13	2020-03-20	500	1000	EFOSC2	13.27	13.10	12.79
VOS 431	509013483546651008		01:35:45.07	+58:14:21.3	2019-09-05		1200; 900		CAFOS	14.42	13.98	13.33
VOS 445	5546155247158673792		08:03:47.18	-33:14:43.9	2020-03-13	2020-03-21	900	1800	EFOSC2	14.07	13.59	12.86
VOS 448	2012261211191786624		23:40:27.98	+61:02:00.5	2019-08-08	2019-08-10	1200	1000	IDS	14.29	13.54	12.66
VOS 458	5334867393402370816		11:45:01.63	-62:11:49.2	2020-03-12	2020-03-19	1500	2200	EFOSC2	14.28	13.08	12.00
VOS 461	5868283055734381184	THA 17-31	13:18:12.45	-62:43:39.6	2020-03-12	2020-03-20	600	1200	EFOSC2	13.48	13.24	12.81
VOS 465	3045350894857953664		07:09:27.89	-12:12:16.0	2020-03-12	2020-03-19	1000	2200	EFOSC2	13.49	13.17	12.68
VOS 473	2203217037728935296	V623 Cep	21:59:06.12	+60:40:53.3	2019-09-04		500		CAFOS	12.65	12.45	12.08
VOS 475	2004435162317441280		22:11:13.13	+52:53:34.1	2019-08-08	2019-08-11	600	1000	IDS	13.30	13.17	12.92
VOS 476	5868479043676144384		13:19:09.85	-62:25:09.2	2020-03-12	2020-03-20	600	1200	EFOSC2	13.71	13.44	12.96
VOS 481	2019217237173395968		19:25:14.20	+22:40:38.2	2019-09-03		600		CAFOS	13.99	13.29	12.47
VOS 482	5338434587073245056	SPH 103	10:52:59.79	-59:12:34.8	2020-03-13	2020-03-21	900	1800	EFOSC2	14.25	14.05	13.70
VOS 491	5866408555870965632		14:08:42.48	-61:10:42.6	2020-03-12	2020-03-19	800	800	EFOSC2	13.91	13.64	13.20
VOS 495	4153689436387288448		18:18:30.84	-11:48:34.5	2019-08-04	2019-08-09	600	800	IDS	13.81	12.93	11.99
VOS 519	5858981977697486592		13:06:34.80	-65:04:09.2	2020-03-13	2020-03-21	900	1800	EFOSC2	14.08	13.94	13.69
VOS 522	2164554394961279360		21:20:03.23	+46:57:46.7	2019-09-04		600		CAFOS	13.36	12.93	12.31
VOS 588	466147613983225472	GGA 216	02:59:05.13	+60:54:04.1	2019-08-07	2019-08-08	900	1200	IDS	13.45	12.96	12.25
VOS 595	181458215025292160	MWC 485	05:14:26.92	+32:48:03.2	2019-09-06		1200		CAFOS	12.39	12.09	11.59
VOS 603	506799479443438080	TZ Per	02:13:50.96	+58:22:52.2	2019-09-06		1600		CAFOS	13.82	13.58	13.09
VOS 668	5258744904832986880		10:15:19.02	-57:30:57.4	2020-03-12	2020-03-21	1200	1800	EFOSC2	13.88	13.69	13.32
VOS 672	2013834955933319680		23:16:07.57	+60:01:43.7	2019-08-07	2019-08-10	750	1000	IDS	13.94	13.23	12.34
VOS 689	426213008067891968		01:06:36.15	+59:46:09.4	2019-08-05	2019-08-12	600	1300	IDS	13.88	13.59	13.11
VOS 703	3045461567573658368		07:14:31.23	-11:29:27.1	2020-03-14	2020-03-19	900	1800	EFOSC2	13.31	12.83	12.15
VOS 738	464675226177231744		02:53:59.02	+60:39:58.6	2019-08-08	2019-08-10	600	2000	IDS	12.99	12.58	11.98
VOS 759	1978002902777895552		21:40:03.13	+48:02:10.5	2019-09-06		900; 600		CAFOS	12.68	12.25	11.64
VOS 787	430481140413947520		00:23:13.67	+61:59:31.9	2019-09-06		1600		CAFOS	13.90	13.43	12.77
VOS 821	2199663691020796928		22:10:29.25	+58:49:00.3	2019-09-05		1200; 800		CAFOS	13.42	12.59	11.69
VOS 854	4097384579759711744		18:17:12.00	-16:56:01.7	2020-03-13	2020-03-21	600	1000	EFOSC2	13.25	12.81	12.19
VOS 879	2007423050801656960		22:47:40.11	+58:09:03.6	2019-09-06		1600		CAFOS	13.73	13.33	12.72
VOS 898	258477905042591488		04:30:16.24	+48:52:09.9	2019-09-04		800		CAFOS	13.50	12.93	12.17
VOS 911	5935057668182928256		16:16:05.33	-50:46:03.7	2020-03-14	2020-03-19	600	1200	EFOSC2	12.78	12.46	11.95
VOS 934	442287245287225856		03:28:32.63	+51:13:54.4	2019-09-06		1400		CAFOS	13.06	12.55	11.85
VOS 941	5543776728634411008		08:23:01.90	-33:50:42.4	2020-03-13	2020-03-19	450	1000	EFOSC2	12.75	12.46	12.01
VOS 949	523968761523650304		00:49:47.54	+63:38:10.0	2019-09-05		900		CAFOS	13.18	12.69	12.01

Table B1
(Continued)

Name	Gaia EDR3 source id	Alternative name	R.A. hh:mm:ss	Decl. dd:mm:ss.s	Obs Date		Exposure Time		Spectrograph	G_{BP} [mag]	G [mag]	G_{RP} [mag]
					Blue	Red	Blue [s]	Red [s]				
VOS 953	4097686082159430784		18:16:49.66	-16:03:16.2	2020-03-14	2020-03-21	1500	1800	EFOSC2	13.82	13.18	12.40
VOS 983	5966697730168623488	[MP69] 4	16:57:26.67	-40:25:56.3	2020-03-13	2020-03-20	600	1200	EFOSC2	13.61	13.39	13.00
VOS 1026	2014090042628166656		23:12:26.37	+60:58:12.9	2019-08-05	2019-08-09	300	900	IDS	12.40	12.14	11.70
VOS 1034	4098138462472816384	SS 369	18:22:44.15	-15:33:09.0	2019-08-04	2019-08-10	600	1000	IDS	13.86	12.76	11.71
VOS 1045	2173413297587679744		21:43:57.03	+53:03:14.2	2019-09-06		1200; 800		CAFOS	12.83	12.43	11.86
VOS 1126	2013507915639151488	CDS 5176	22:58:59.08	+59:18:02.3	2019-09-05		800		CAFOS	13.67	13.15	12.43
VOS 1139	462017332914172800		03:14:22.91	+59:14:57.0	2019-09-05		1200		CAFOS	14.11	13.55	12.81
VOS 1152	2020089630912890368		19:43:04.40	+23:18:48.6	2019-08-05	2019-08-10	600	900	IDS	13.89	13.47	12.83
VOS 1225	462339210641162496		03:31:56.87	+60:07:37.7	2019-09-06		700; 700		CAFOS	12.35	12.03	11.53
VOS 1240	1828276425855506304		19:47:39.86	+23:26:39.2	2019-09-05		800; 800		CAFOS	13.50	12.53	11.56
VOS 1245	5854532425868957184		14:18:51.43	-61:24:37.8	2020-03-13	2020-03-21	1500	1800	EFOSC2	14.31	13.93	13.36
VOS 1258	5338316767522194688		10:56:50.81	-60:14:22.7	2020-03-14	2020-03-21	1200	1600	EFOSC2	14.11	13.79	13.26
VOS 1276	2005453516247868416		22:09:29.67	+54:21:27.2	2019-09-04		400		CAFOS	12.84	12.71	12.47
VOS 1331	2066412811690449792		20:38:45.88	+42:07:04.7	2019-08-08	2019-08-11	1000	1200	IDS	14.85	13.67	12.56
VOS 1336	5333545642950621696		11:37:46.97	-63:42:56.4	2020-03-13	2020-03-21	900	1200	EFOSC2	13.73	13.40	12.67
VOS 1342	4272195138879459200	LkHA 348	18:34:12.65	-00:26:21.8	2019-08-07	2019-08-09	900	750	IDS	14.26	13.00	11.87
VOS 1380	2035402872974695936	IU Cyg	19:50:08.24	+34:09:57.5	2019-08-06	2019-08-11	900	900	IDS	13.67	12.95	12.11
VOS 1385	4090478474203479296		18:15:59.52	-22:41:38.0	2019-08-05	2019-08-08	900	900	IDS	16.54	15.22	14.24
VOS 1405	5254137160888722816	THA 35-II-79	10:39:15.05	-60:50:17.2	2020-03-13	2020-03-20	600	1200	EFOSC2	13.14	12.94	12.54
VOS 1407	4155634296310906112		18:37:48.95	-09:03:34.5	2019-08-05	2019-08-11	900	1500	IDS	14.47	13.87	13.10
VOS 1424	4265423830878562944		18:53:48.18	-00:37:29.9	2019-08-06	2019-08-08	1000	1200	IDS	15.63	14.79	13.84
VOS 1440	514573743903855616	VES 723	02:14:48.42	+62:26:22.3	2019-08-05	2019-08-08	450	300	IDS	13.45	12.97	12.22
VOS 1515	4152405172406857088		18:22:00.12	-13:48:55.6	2019-08-07	2019-08-09	1200	900	IDS	15.23	13.81	12.63
VOS 1575	2014636396825359488		22:54:15.84	+60:47:49.4	2019-08-08	2019-08-12	1200	1300	IDS	15.57	14.28	13.13
VOS 1600	4152422554127130240		18:20:58.12	-13:40:32.4	2019-08-05	2019-08-11	600	1300	IDS	12.89	12.11	11.22
VOS 1617	4094703381988286592	SS 352	18:13:13.57	-19:24:08.5	2019-08-04	2019-08-09	300	750	IDS	12.98	12.46	11.77
VOS 1634	2071705173505640448		19:54:28.06	+36:26:08.1	2019-09-05		900; 900		CAFOS	13.71	11.34	9.96
VOS 1635	3123854268434443648		06:30:27.36	+01:44:06.3	2020-03-14	2020-03-19	900	1800	EFOSC2	13.62	12.64	11.65
VOS 1672	2061354783350172672	AS 397	20:17:33.47	+38:57:20.1	2019-08-05	2019-08-08	450	900	IDS	13.05	12.46	11.70
VOS 1680	508164248253696384		01:49:38.77	+60:37:09.8	2019-08-07	2019-08-12	1200	1500	IDS	15.04	14.57	13.90
VOS 1771	429587679827887360		00:15:19.69	+61:14:58.1	2019-09-04; 06		300; 600		CAFOS	12.72	12.34	11.76
VOS 1806	431934385541454080		00:20:45.25	+64:30:22.2	2019-09-05		1200; 1200		CAFOS	14.16	12.63	11.45
VOS 1873	4256499816550576256		18:40:50.30	-05:39:41.1	2019-08-06	2019-08-09	450	900	IDS	13.50	12.95	12.21
VOS 1913	2198056166359436160		21:56:51.24	+55:22:46.4	2019-09-04		500		CAFOS	13.10	12.45	11.65
VOS 1922	2066784304885540992		20:51:50.20	+43:19:29.8	2019-08-07	2019-08-10	900	800	IDS	13.70	12.53	11.43
VOS 2047	464144544317484544		02:46:43.96	+59:21:16.8	2019-08-07	2019-08-08	900	600	IDS	13.56	13.10	12.43
VOS 2051	272076905372370816		04:29:17.05	+52:34:26.3	2019-09-05; 06		1200		CAFOS	14.23	13.69	12.95
VOS 2060	1834095999134055680		19:57:55.90	+23:28:25.8	2019-08-07	2019-08-12	300	1200	IDS	12.62	12.18	11.55
VOS 2085	2007419820986293504	LS III+57 89	22:47:45.63	+58:06:48.8	2019-08-08	2019-08-10	450	700	IDS	11.92	11.61	11.09
VOS 2093	5866357054949304832	WRAY 15-1157	13:59:29.93	-61:23:07.7	2020-03-12	2020-03-19	700	1400	EFOSC2	14.01	12.92	11.87
VOS 2098	4259271891523989376		18:50:31.25	-01:24:09.6	2019-08-05	2019-08-11	600	1500	IDS	12.67	12.03	11.22
VOS 2158	1981413759654971008	MWC 645	21:53:27.48	+52:59:58.0	2019-08-05	2019-08-09	450	720	IDS	12.78	12.21	11.32
VOS 2161	6054820460425919616	WRAY 15-966	12:23:13.35	-62:20:06.3	2020-03-13	2020-03-20	1200	2000	EFOSC2	14.11	13.42	12.48
VOS 2164	4318785810234714752	PN Me 1-1	19:39:09.82	+15:56:48.2	2019-08-04	2019-08-09	300	800	IDS	12.50	12.52	11.25
VOS 2169	1980664098879084288	MWC 1051	21:54:21.14	+51:27:53.5	2019-08-06	2019-08-10	450	900	IDS	12.95	12.56	11.95
VOS 2171	2200017424528999936		22:23:29.69	+57:37:49.0	2019-08-06	2019-08-11	900	1000	IDS	14.68	13.88	12.96
VOS 2196	205118464010485632	MWC 482	05:01:20.31	+43:32:50.7	2019-09-04		400		CAFOS	12.56	12.34	11.91

Table B1
(Continued)

Name	Gaia EDR3 source id	Alternative name	R.A. hh:mm:ss	Decl. dd:mm:ss.s	Obs Date		Exposure Time		Spectrograph	G_{BP} [mag]	G [mag]	G_{RP} [mag]
					Blue	Red	Blue [s]	Red [s]				
VOS 3851	5884829984147822976		15:48:33.09	-54:29:01.6	2020-03-12	2020-03-20	800	1600	EFOSC2	13.93	13.44	12.75
VOS 4439	5544618168572613504		08:08:45.39	-36:08:40.0	2020-03-14	2020-03-21	1200	1200	EFOSC2	14.04	13.12	12.13
VOS 4463	4253225574005033088	FG Sct	18:45:03.63	-06:06:15.3	2020-03-14		233		EFOSC2	13.39	12.74	11.99
VOS 4614	5972078735771910784	WRAY 15-1632	17:11:08.18	-40:31:56.6	2020-03-13	2020-03-20	1200	1200	EFOSC2	13.77	12.74	11.69

Note. Column 1 contains the name of the sources as assigned in this work. Column 2 contains the Gaia EDR3 source identity of each source. Column 3 shows other literature names. Columns 4 and 5 are Gaia EDR3 right ascensions and declinations. Columns 6 and 7 list the observation dates (for the blue and red settings, see Section 2). Columns 8 and 9 present the exposure times. Column 10 states the spectrograph used in each case. Columns 11 to 13 show the Gaia magnitudes. See Table 1 for details on the instrumental setups used at each telescope.

(This table is available in its entirety in machine-readable form.)

Table B2
Stellar Parameters, Distances and Extinctions (A_V) for the 145 Observed Sources, Ordered by Name

Name	SpType	T_{eff} [K]	Distance [pc]	A_V [mag]	$\log(L [L_{\odot}])$	Radius [R_{\odot}]	Mass [M_{\odot}]	Age [Myr]	Remarks
VOS 4	A0	10, 000 ⁺⁵⁰⁰ ₋₅₀₀	932 ⁺¹⁹ ₋₁₈	1.813 ^{+0.083} _{-0.086}	1.356 ^{+0.089} _{-0.092}	1.59 ^{+0.36} _{-0.29}	2.14 ^{+0.13} _{-0.14}	9 ⁺²⁸ ₋₃	
VOS 7	F2–F8	6500 ⁺⁵⁰⁰ ₋₅₀₀	472.4 ^{+4.0} _{-3.9}	1.79 ^{+0.26} _{-0.28}	0.61 ^{+0.11} _{-0.11}	1.60 ^{+0.54} _{-0.39}	1.34 ^{+0.26} _{-0.07}	15 ⁺³⁵ ₋₇	
VOS 15	A6	8000 ⁺⁵⁰⁰ ₋₅₀₀	1119 ⁺²⁷ ₋₂₆	1.76 ^{+0.19} _{-0.22}	1.16 ^{+0.12} _{-0.12}	1.98 ^{+0.61} _{-0.46}	1.81 ^{+0.25} _{-0.14}	8.0 ^{+4.6} _{-1.5}	
VOS 20	A9	7440 ⁺⁶⁰ ₋₂₄₀	813 ⁺¹³ ₋₁₃	2.81 ^{+0.01} _{-0.10}	0.964 ^{+0.028} _{-0.059}	1.83 ^{+0.19} _{-0.15}	1.63 ^{+0.11} _{-0.05}	10.21 ^{+0.76} _{-0.49}	
VOS 22	B8	12, 500 ⁺²⁵⁰⁰ ₋₂₅₀₀	2409 ⁺⁶³ ₋₆₀	2.50 ^{+0.13} _{-0.26}	2.98 ^{+0.25} _{-0.32}	6.6 ^{+7.2} _{-3.4}	5.5 ^{+2.1} _{-1.4}	0.41 ^{+0.62} _{-0.28}	
VOS 24	G0	5920 ⁺¹²⁰ ₋₄₀	566.1 ^{+9.3} _{-9.0}	2.418 ^{+0.075} _{-0.033}	0.897 ^{+0.040} _{-0.023}	2.67 ^{+0.16} _{-0.17}	1.93 ^{+0.07} _{-0.14}	4.7 ^{+1.3} _{-0.4}	
VOS 26	A2	9000 ⁺¹⁰⁰⁰ ₋₁₀₀₀	2402 ⁺⁹² ₋₈₅	1.73 ^{+0.22} _{-0.32}	2.03 ^{+0.19} _{-0.21}	4.3 ^{+2.5} _{-1.6}	3.12 ^{+0.85} _{-0.59}	1.9 ^{+1.6} _{-1.0}	
VOS 32	G0	5920 ⁺¹²⁰ ₋₄₀	1155 ⁺²⁵ ₋₂₄	3.005 ^{+0.070} _{-0.031}	1.132 ^{+0.044} _{-0.027}	3.50 ^{+0.23} _{-0.24}	2.31 ^{+0.10} _{-0.16}	2.96 ^{+0.80} _{-0.33}	
VOS 35	F	6500 ⁺¹⁰⁰⁰ ₋₁₀₀₀	718.0 ^{+5.6} _{-5.5}	2.38 ^{+0.48} _{-0.59}	1.07 ^{+0.21} _{-0.21}	2.7 ^{+2.1} _{-1.1}	1.8 ^{+1.2} _{-0.3}	6.8 ^{+6.4} _{-5.8}	
VOS 42	B	21, 000 ^{+10,000} _{-10,000}	764 ⁺¹⁰ ₋₁₀	4.71 ^{+0.43} _{-0.51}	2.97 ^{+0.52} _{-0.85}	2 ⁺¹³ ₋₂	5.8 ^{+3.2} _{-2.8}	0.7 ^{+7.1} _{-0.6}	
VOS 48	G0	5920 ⁺¹²⁰ ₋₄₀	900 ⁺¹⁶ ₋₁₆	2.186 ^{+0.077} _{-0.034}	0.891 ^{+0.042} _{-0.024}	2.65 ^{+0.17} _{-0.17}	1.91 ^{+0.09} _{-0.12}	4.9 ^{+1.2} _{-0.6}	
VOS 50	K5	4500 ⁺⁵⁰⁰ ₋₅₀₀	642 ⁺¹⁷ ₋₁₆	1.0 ^{+0.7} _{-1.0}	-0.27 ^{+0.17} _{-0.24}	1.20 ^{+0.66} _{-0.46}	1.00 ^{+0.15} _{-0.33}	8 ⁺³⁸ ₋₇	T Tau
VOS 51	B7	14, 000 ⁺⁵⁰⁰ ₋₁₅₀₀	796.3 ^{+8.1} _{-8.0}	2.538 ^{+0.035} _{-0.071}	2.12 ^{+0.06} _{-0.15}	1.96 ^{+0.67} _{-0.42}	3.40 ^{+0.19} _{-0.47}	2.7 ^{+7.6} _{-0.5}	
VOS 55	G9–K4	5000 ⁺⁵⁰⁰ ₋₅₀₀	1419 ⁺¹⁴ ₋₂₄	0.77 ^{+0.40} _{-0.72}	0.92 ^{+0.12} _{-0.18}	3.9 ^{+1.6} _{-1.3}	1.9 ^{+0.7} _{-1.0}	0.6 ^{+2.4} _{-0.5}	
VOS 56	A4	8270 ⁺²⁸⁰ ₋₁₉₀	878 ⁺²⁰ ₋₂₀	2.44 ^{+0.14} _{-0.05}	1.405 ^{+0.081} _{-0.057}	2.45 ^{+0.37} _{-0.30}	2.02 ^{+0.13} _{-0.07}	5.9 ^{+0.6} _{-1.0}	
VOS 63	F0	7200 ⁺²⁴⁰ ₋₁₇₀	1770 ⁺⁴⁷ ₋₄₄	4.633 ^{+0.087} _{-0.086}	2.494 ^{+0.066} _{-0.055}	11.4 ^{+1.5} _{-1.4}	5.39 ^{+0.32} _{-0.34}	0.306 ^{+0.087} _{-0.058}	Young
VOS 67	G0	5920 ⁺¹²⁰ ₋₄₀	2586 ⁺⁸¹ ₋₇₆	2.768 ^{+0.072} _{-0.032}	2.620 ^{+0.052} _{-0.035}	19.4 ^{+1.5} _{-1.5}	6.40 ^{+0.18} _{-0.14}	0.125 ^{+0.013} _{-0.013}	Young
VOS 69	A3	8500 ⁺⁵⁰⁰ ₋₅₀₀	683.1 ^{+8.9} _{-8.6}	2.77 ^{+0.12} _{-0.19}	1.08 ^{+0.09} _{-0.11}	1.60 ^{+0.41} _{-0.34}	1.80 ^{+0.22} _{-0.10}	11 ⁺³⁹ ₋₄	
VOS 70	A7	7800 ⁺²⁰⁰ ₋₃₀₀	1150 ⁺³⁰ ₋₂₈	4.02 ^{+0.10} _{-0.10}	2.221 ^{+0.071} _{-0.069}	7.1 ^{+1.2} _{-1.2}	4.07 ^{+0.35} _{-0.27}	0.81 ^{+0.20} _{-0.20}	
VOS 76	A8	7500 ⁺⁵⁰⁰ ₋₅₀₀	1831 ⁺⁴⁹ ₋₄₇	1.73 ^{+0.22} _{-0.24}	1.71 ^{+0.12} _{-0.12}	4.2 ^{+1.9} _{-1.0}	2.70 ^{+0.44} _{-0.36}	2.6 ^{+1.3} _{-0.9}	
VOS 77	G9–K4	5000 ⁺⁵⁰⁰ ₋₅₀₀	362.9 ^{+2.4} _{-2.4}	0.83 ^{+0.40} _{-0.72}	0.20 ^{+0.11} _{-0.17}	1.69 ^{+0.69} _{-0.54}	1.43 ^{+0.12} _{-0.50}	5 ⁺¹³ ₋₄	
VOS 78	A9	7440 ⁺⁶⁰ ₋₂₄₀	1597 ⁺⁶⁸ ₋₆₂	1.56 ^{+0.01} _{-0.11}	1.285 ^{+0.050} _{-0.082}	2.64 ^{+0.35} _{-0.28}	1.93 ^{+0.11} _{-0.11}	6.3 ^{+1.1} _{-0.9}	
VOS 84	A8	7500 ⁺⁵⁰⁰ ₋₅₀₀	1146 ⁺²¹ ₋₂₀	1.31 ^{+0.22} _{-0.25}	1.11 ^{+0.12} _{-0.12}	2.11 ^{+0.66} _{-0.49}	1.71 ^{+0.19} _{-0.10}	8.8 ^{+2.9} _{-2.3}	
VOS 95	A0	9500 ⁺⁵⁰⁰ ₋₅₀₀	1205 ⁺²⁹ ₋₂₈	1.96 ^{+0.09} _{-0.13}	1.75 ^{+0.10} _{-0.11}	2.78 ^{+0.68} _{-0.56}	2.44 ^{+0.23} _{-0.15}	3.79 ^{+0.70} _{-0.89}	
VOS 104	A2	8840 ⁺³⁶⁰ ₋₂₉₀	804.7 ^{+8.5} _{-8.4}	2.02 ^{+0.12} _{-0.04}	1.354 ^{+0.080} _{-0.045}	2.03 ^{+0.35} _{-0.25}	2.07 ^{+0.22} _{-0.10}	6.0 ^{+1.6} _{-0.9}	
VOS 105	F5	6510 ⁺¹³⁰ ₋₁₇₀	1886 ⁺⁶⁶ ₋₆₂	2.94 ^{+0.06} _{-0.10}	1.616 ^{+0.055} _{-0.062}	5.05 ^{+0.63} _{-0.53}	2.84 ^{+0.17} _{-0.20}	2.04 ^{+0.48} _{-0.34}	
VOS 108	A0	9500 ⁺⁵⁰⁰ ₋₅₀₀	2665 ⁺⁹⁰ ₋₈₄	1.64 ^{+0.09} _{-0.13}	2.10 ^{+0.10} _{-0.13}	4.1 ^{+1.0} _{-1.0}	3.18 ^{+0.37} _{-0.33}	1.85 ^{+0.70} _{-0.52}	
VOS 111	A0	9700 ⁺¹⁰⁰⁰ ₋₅₀₀	1372 ⁺³⁰ ₋₂₈	4.32 ^{+0.17} _{-0.10}	2.06 ^{+0.16} _{-0.10}	3.8 ^{+1.3} _{-1.0}	3.04 ^{+0.51} _{-0.31}	2.12 ^{+0.83} _{-0.77}	
VOS 112	G	5500 ⁺⁵⁰⁰ ₋₅₀₀	2480 ⁺⁹¹ ₋₈₅	2.56 ^{+0.30} _{-0.35}	1.98 ^{+0.13} _{-0.13}	10.8 ^{+4.4} _{-3.0}	4.63 ^{+0.56} _{-0.84}	0.29 ^{+0.42} _{-0.22}	
VOS 118	G	5750 ⁺⁵⁰⁰ ₋₅₀₀	677.9 ^{+6.0} _{-5.9}	0.98 ^{+0.33} _{-0.35}	0.36 ^{+0.12} _{-0.11}	1.53 ^{+0.58} _{-0.39}	1.31 ^{+0.41} _{-0.19}	12 ⁺¹¹ ₋₉	
VOS 121	B9.5	10, 400 ⁺¹²⁰⁰ ₋₁₀₀₀	905.9 ^{+9.3} _{-9.1}	2.12 ^{+0.14} _{-0.16}	1.46 ^{+0.16} _{-0.15}	1.64 ^{+0.75} _{-0.53}	2.26 ^{+0.32} _{-0.23}	8 ⁺²⁶ ₋₄	
VOS 125	B3	17, 500 ⁺²⁵⁰⁰ ₋₂₅₀₀	3110 ⁺¹⁶⁰ ₋₁₄₀	3.92 ^{+0.08} _{-0.14}	3.63 ^{+0.21} _{-0.25}	7.1 ^{+5.3} _{-3.1}	8.2 ^{+2.0} _{-1.5}	0.15 ^{+0.14} _{-0.08}	
VOS 131	F6–G4	6000 ⁺⁵⁰⁰ ₋₅₀₀	667.8 ^{+6.4} _{-6.3}	1.12 ^{+0.29} _{-0.36}	0.86 ^{+0.11} _{-0.12}	2.48 ^{+0.88} _{-0.65}	1.79 ^{+0.66} _{-0.35}	6.0 ^{+6.1} _{-4.1}	
VOS 135	G0	5920 ⁺¹²⁰ ₋₄₀	3580 ⁺²²⁰ ₋₂₀₀	1.316 ^{+0.083} _{-0.037}	1.765 ^{+0.079} _{-0.059}	7.25 ^{+0.80} _{-0.74}	3.63 ^{+0.22} _{-0.21}	0.86 ^{+0.20} _{-0.14}	
VOS 136	G	5750 ⁺⁵⁰⁰ ₋₅₀₀	472.6 ^{+4.3} _{-4.3}	1.81 ^{+0.31} _{-0.32}	0.64 ^{+0.12} _{-0.11}	2.10 ^{+0.78} _{-0.53}	1.68 ^{+0.45} _{-0.38}	6.3 ^{+8.9} _{-4.5}	
VOS 140	B9.5	10, 400 ⁺¹²⁰⁰ ₋₁₀₀₀	2440 ⁺¹³⁰ ₋₁₂₀	1.81 ^{+0.14} _{-0.16}	1.53 ^{+0.20} _{-0.19}	1.79 ^{+0.93} _{-0.63}	2.27 ^{+0.48} _{-0.21}	6 ⁺²⁵ ₋₃	
VOS 164	A7	7800 ⁺²⁰⁰ ₋₃₀₀	1936 ⁺⁷¹ ₋₆₇	0.84 ^{+0.11} _{-0.11}	1.185 ^{+0.083} _{-0.081}	2.14 ^{+0.41} _{-0.29}	1.78 ^{+0.10} _{-0.07}	8.0 ^{+0.8} _{-1.2}	
VOS 184	A0	9700 ⁺¹⁰⁰⁰ ₋₅₀₀	2760 ⁺¹⁴⁰ ₋₁₃₀	2.67 ^{+0.17} _{-0.10}	1.92 ^{+0.19} _{-0.12}	3.2 ^{+1.2} _{-0.9}	2.73 ^{+0.52} _{-0.24}	2.8 ^{+0.9} _{-1.1}	
VOS 199	F1	7000 ⁺⁵⁰⁰ ₋₅₀₀	1014 ⁺²¹ ₋₂₀	0.60 ^{+0.26} _{-0.29}	0.83 ^{+0.12} _{-0.13}	1.77 ^{+0.59} _{-0.44}	1.51 ^{+0.23} _{-0.11}	12 ⁺³⁸ ₋₄	
VOS 200	A0	10, 000 ⁺¹⁰⁰⁰ ₋₁₀₀₀	2420 ⁺¹¹⁰ ₋₁₀₀	3.52 ^{+0.15} _{-0.21}	2.88 ^{+0.18} _{-0.20}	9.1 ^{+4.7} _{-3.1}	5.8 ^{+1.4} _{-1.1}	0.31 ^{+0.31} _{-0.17}	
VOS 209	F9	6000 ⁺²⁵⁰ ₋₂₅₀	649.4 ^{+6.7} _{-6.5}	0.60 ^{+0.21} _{-0.21}	0.314 ^{+0.058} _{-0.076}	1.33 ^{+0.22} _{-0.21}	1.17 ^{+0.15} _{-0.06}	18.7 ^{+4.9} _{-6.6}	T Tau
VOS 215	B9.5	10, 500 ⁺⁵⁰⁰ ₋₅₀₀	1513 ⁺³⁶ ₋₃₄	1.652 ^{+0.069} _{-0.083}	1.676 ^{+0.085} _{-0.091}	2.08 ^{+0.45} _{-0.37}	2.60 ^{+0.20} _{-0.26}	4.0 ^{+1.8} _{-0.9}	
VOS 224	A0	10, 000 ⁺⁵⁰⁰ ₋₅₀₀	1647 ⁺³⁸ ₋₃₆	1.583 ^{+0.083} _{-0.086}	1.788 ^{+0.091} _{-0.094}	2.61 ^{+0.60} _{-0.48}	2.48 ^{+0.25} _{-0.13}	3.74 ^{+0.48} _{-0.73}	
VOS 233	A8	7500 ⁺⁵⁰⁰ ₋₅₀₀	2289 ⁺⁷² ₋₆₈	1.03 ^{+0.22} _{-0.25}	1.59 ^{+0.13} _{-0.13}	3.7 ^{+1.2} _{-0.9}	2.47 ^{+0.42} _{-0.33}	3.5 ^{+1.7} _{-1.2}	
VOS 247	B9.5	10, 400 ⁺¹²⁰⁰ ₋₁₀₀₀	2537 ⁺⁷⁹ ₋₇₅	2.01 ^{+0.14} _{-0.16}	2.22 ^{+0.18} _{-0.17}	4.0 ^{+1.9} _{-1.3}	3.32 ^{+0.70} _{-0.43}	1.72 ^{+0.88} _{-0.77}	
VOS 250	A3	8500 ⁺⁵⁰⁰ ₋₅₀₀	1128 ⁺²⁹ ₋₂₈	1.34 ^{+0.12} _{-0.20}	1.38 ^{+0.10} _{-0.12}	2.25 ^{+0.61} _{-0.51}	1.99 ^{+0.23} _{-0.13}	6.3 ^{+1.9} _{-1.3}	
VOS 253	A0	9500 ⁺⁵⁰⁰ ₋₅₀₀	1286 ⁺²³ ₋₂₂	1.08 ^{+0.09} _{-0.13}	1.35 ^{+0.09} _{-0.10}	1.75 ^{+0.41} _{-0.35}	2.07 ^{+0.27} _{-0.11}	8 ⁺³⁰ ₋₃	
VOS 271	A3	8500 ⁺⁵⁰⁰ ₋₅₀₀	2012 ⁺⁷⁰ ₋₆₅	2.58 ^{+0.12} _{-0.19}	1.89 ^{+0.11} _{-0.13}	4.1 ^{+1.2} _{-0.9}	2.90 ^{+0.38} _{-0.35}	2.3 ^{+1.0} _{-0.7}	
VOS 274	A3	8500 ⁺⁵⁰⁰ ₋₅₀₀	789 ⁺¹⁰ ₋₉	2.05 ^{+0.12} _{-0.19}	1.22 ^{+0.09} _{-0.11}	1.88 ^{+0.48} _{-0.40}	2.06 ^{+0.12} _{-0.25}	6.6 ^{+6.5} _{-0.7}	
VOS 284	A7	7750 ⁺⁵⁰⁰ ₋₅₀₀	1104 ⁺²⁰ ₋₂₀	1.36 ^{+0.20} _{-0.19}	1.45 ^{+0.12} _{-0.11}	2.96 ^{+0.91} _{-0.65}	2.15 ^{+0.30} _{-0.20}	4.8 ^{+1.6} _{-1.5}	
VOS 290	B2	20, 600 ⁺⁵⁴⁰⁰ ₋₃₆₀₀	2760 ⁺¹¹⁰ ₋₁₀₀	3.55 ^{+0.33} _{-0.12}	3.76 ^{+0.37} _{-0.27}	5.9 ^{+7.5} _{-3.2}	8.7 ^{+3.5} _{-1.5}	0.14 ^{+0.58} _{-0.09}	
VOS 293	B8	12, 000 ⁺¹⁰⁰⁰ ₋₁₀₀₀	2326 ⁺⁶⁵ ₋₆₁	1.341 ^{+0.060} _{-0.072}	2.11 ^{+0.12} _{-0.13}	2.6 ^{+1.0} _{-0.7}	3.14 ^{+0.54} _{-0.34}	2.2 ^{+6.9} _{-0.6}	
VOS 297	F1	7000 ⁺⁵⁰⁰ ₋₅₀₀	1725 ⁺³⁷ ₋₃₆	1.89 ^{+0.24} _{-0.27}	1.57 ^{+0.12} _{-0.12}	4.1 ^{+1.4} _{-1.0}	2.54 ^{+0.46} _{-0.35}	2.9 ^{+1.6} _{-1.2}	
VOS 321	A8	7500 ⁺⁵⁰⁰ ₋₅₀₀	966 ⁺¹⁰ ₋₁₀	0.92 ^{+0.23} _{-0.26}	1.12 ^{+0.11} _{-0.11}	2.14 ^{+0.65} _{-0.49}	1.72 ^{+0.18} _{-0.10}	8.6 ^{+2.6} _{-2.4}	
VOS 336	F6–G4	6000 ⁺⁵⁰⁰ ₋₅₀₀	688.4 ^{+5.9} _{-5.8}	1.94 ^{+0.27} _{-0.33}	1.03 ^{+0.11} _{-0.12}	3.0 ^{+1.1} _{-0.8}	2.06 ^{+0.68} _{-0.42}	4.2 ^{+4.5} _{-2.7}	
VOS 341	A0	10, 000 ⁺¹⁰⁰⁰ ₋₁₀₀₀	2229 ⁺⁶⁸ ₋₆₄	1.46 ^{+0.15} _{-0.22}	1.68 ^{+0.16} _{-0.19}	2.3 ^{+1.1} _{-0.8}	2.45 ^{+0.47} _{-0.31}	4 ⁺²⁴ ₋₁	
VOS 361	A8	7500 ⁺⁵⁰⁰ ₋₅₀₀	1128 ⁺¹⁸ ₋₁₇	1.04 ^{+0.22} _{-0.25}	1.23 ^{+0.12} _{-0.12}	2.45 ^{+0.76} _{-0.57}	1.85 ^{+0.25} _{-0.13}	7.1 ^{+1.5} _{-2.2}	
VOS 373	A3	8500 ⁺⁵⁰⁰ ₋₅₀₀	1444 ⁺³⁶ ₋₃₄	1.74 ^{+0.12} _{-0.20}	1.90 ^{+0.10} _{-0.12}	4.1 ^{+1.1} _{-0.9}	2.90 ^{+0.36} _{-0.34}	2.3 ^{+1.0} _{-0.7}	

Table B2
(Continued)

Name	SpType	T_{eff} [K]	Distance [pc]	A_V [mag]	$\log(L [L_{\odot}])$	Radius [R_{\odot}]	Mass [M_{\odot}]	Age [Myr]	Remarks
VOS 398	G	5500^{+500}_{-500}	$759.8^{+6.5}_{-6.4}$	$0.49^{+0.37}_{-0.43}$	$0.37^{+0.12}_{-0.12}$	$1.69^{+0.67}_{-0.46}$	$1.47^{+0.28}_{-0.34}$	8^{+13}_{-6}	
VOS 406	K4–K9	4250^{+500}_{-500}	$332.5^{+1.3}_{-1.3}$	$0.00^{+0.83}_{-0.00}$	$-0.16^{+0.18}_{-0.10}$	$1.54^{+0.89}_{-0.37}$	$0.76^{+0.47}_{-0.33}$	$2.2^{+6.4}_{-1.7}$	T Tau
VOS 413	B9	$11,000^{+1000}_{-1000}$	2313^{+64}_{-61}	$1.27^{+0.07}_{-0.15}$	$2.04^{+0.13}_{-0.16}$	$2.9^{+1.2}_{-0.9}$	$2.86^{+0.44}_{-0.25}$	$2.66^{+0.95}_{-0.86}$	
VOS 431	A8	7500^{+500}_{-500}	2330^{+100}_{-90}	$1.68^{+0.22}_{-0.24}$	$1.60^{+0.14}_{-0.14}$	$3.7^{+1.3}_{-0.9}$	$2.47^{+0.43}_{-0.34}$	$3.3^{+1.7}_{-1.2}$	
VOS 445	B9	$11,000^{+1000}_{-1000}$	3600^{+170}_{-160}	$2.83^{+0.07}_{-0.15}$	$2.81^{+0.15}_{-0.18}$	$7.0^{+3.0}_{-2.2}$	$5.2^{+1.0}_{-0.9}$	$0.47^{+0.37}_{-0.21}$	
VOS 448	B1.5	$24,800^{+4200}_{-6300}$	3740^{+180}_{-160}	$4.37^{+0.21}_{-0.24}$	$4.21^{+0.26}_{-0.41}$	7^{+10}_{-4}	$12.3^{+3.7}_{-3.3}$	$0.06^{+0.38}_{-0.04}$	Dubious
VOS 458	G	5500^{+500}_{-500}	3570^{+150}_{-140}	$3.35^{+0.28}_{-0.32}$	$2.81^{+0.13}_{-0.13}$	28^{+12}_{-8}			Cont
VOS 461	A0	$10,000^{+1000}_{-1000}$	1929^{+50}_{-48}	$1.53^{+0.15}_{-0.22}$	$1.85^{+0.16}_{-0.18}$	$2.8^{+1.3}_{-0.9}$	$2.57^{+0.44}_{-0.25}$	$3.4^{+1.7}_{-1.4}$	
VOS 465	A7	7750^{+500}_{-500}	1180^{+23}_{-22}	$1.17^{+0.21}_{-0.20}$	$1.15^{+0.12}_{-0.11}$	$2.09^{+0.64}_{-0.46}$	$1.77^{+0.20}_{-0.11}$	$8.3^{+3.1}_{-2.1}$	
VOS 473	A0	$10,000^{+1000}_{-1000}$	$894.8^{+8.8}_{-8.7}$	$1.31^{+0.15}_{-0.22}$	$1.41^{+0.14}_{-0.17}$	$1.69^{+0.77}_{-0.54}$	$2.14^{+0.36}_{-0.19}$	8^{+30}_{-3}	
VOS 475	B9.5	$10,400^{+1200}_{-1000}$	3760^{+190}_{-170}	$0.98^{+0.13}_{-0.16}$	$2.27^{+0.19}_{-0.18}$	$4.2^{+2.1}_{-1.5}$	$3.48^{+0.78}_{-0.54}$	$1.5^{+1.0}_{-0.7}$	
VOS 476	B9	$11,000^{+2000}_{-2000}$	1940^{+50}_{-47}	$1.84^{+0.13}_{-0.37}$	$1.97^{+0.23}_{-0.32}$	$2.7^{+2.5}_{-1.3}$	$2.79^{+0.81}_{-0.49}$	3^{+20}_{-2}	
VOS 481	F6–G4	6000^{+500}_{-500}	$521.4^{+3.6}_{-3.5}$	$1.87^{+0.27}_{-0.33}$	$0.59^{+0.11}_{-0.12}$	$1.83^{+0.63}_{-0.46}$	$1.45^{+0.50}_{-0.20}$	$10.4^{+7.7}_{-6.9}$	
VOS 482	A0	9500^{+500}_{-500}	2347^{+87}_{-81}	$1.19^{+0.09}_{-0.13}$	$1.52^{+0.11}_{-0.11}$	$2.12^{+0.55}_{-0.45}$	$2.30^{+0.26}_{-0.19}$	$4.8^{+2.8}_{-0.9}$	
VOS 491	A2	9000^{+1000}_{-1000}	2131^{+87}_{-72}	$1.39^{+0.22}_{-0.31}$	$1.63^{+0.20}_{-0.21}$	$2.7^{+1.6}_{-1.0}$	$2.29^{+0.55}_{-0.27}$	$4.4^{+3.0}_{-2.0}$	Dubious
VOS 495	B1.5	$24,800^{+4200}_{-6300}$	1906^{+71}_{-66}	$4.79^{+0.22}_{-0.24}$	$4.01^{+0.26}_{-0.40}$	$5.5^{+7.7}_{-3.0}$	$10.8^{+3.5}_{-3.0}$	$0.09^{+0.63}_{-0.05}$	Dubious
VOS 519	A7	7750^{+500}_{-500}	2267^{+80}_{-75}	$0.25^{+0.21}_{-0.21}$	$1.07^{+0.13}_{-0.12}$	$1.90^{+0.63}_{-0.44}$	$1.74^{+0.24}_{-0.12}$	$8.9^{+7.4}_{-1.7}$	
VOS 522	F1	7000^{+500}_{-500}	$742.4^{+7.4}_{-7.2}$	$1.34^{+0.25}_{-0.28}$	$0.88^{+0.11}_{-0.12}$	$1.88^{+0.60}_{-0.45}$	$1.54^{+0.20}_{-0.10}$	11^{+10}_{-3}	
VOS 588	B8	$12,500^{+1500}_{-1800}$	2190^{+100}_{-90}	$2.91^{+0.07}_{-0.13}$	$2.77^{+0.18}_{-0.22}$	$5.2^{+3.5}_{-2.0}$	$4.7^{+1.1}_{-0.8}$	$0.67^{+0.57}_{-0.34}$	
VOS 595	B9	$11,000^{+1000}_{-1000}$	1990^{+130}_{-120}	$1.96^{+0.07}_{-0.15}$	$2.57^{+0.16}_{-0.19}$	$5.3^{+2.4}_{-1.7}$	$4.28^{+0.87}_{-0.70}$	$0.85^{+0.62}_{-0.39}$	
VOS 603			$456.8^{+4.0}_{-3.9}$						Cont
VOS 668	A0	$10,000^{+500}_{-500}$	2097^{+62}_{-59}	$1.294^{+0.083}_{-0.087}$	$1.65^{+0.10}_{-0.10}$	$2.23^{+0.53}_{-0.43}$	$2.45^{+0.29}_{-0.18}$	$4.1^{+1.9}_{-0.7}$	
VOS 672	B1.5–B8	$18,000^{+7000}_{-7000}$	3130^{+130}_{-120}	$4.07^{+0.29}_{-0.40}$	$3.77^{+0.47}_{-0.67}$	8^{+28}_{-6}	$9.0^{+7.3}_{-3.5}$	$0.1^{+1.5}_{-0.1}$	
VOS 689	B9.5	$10,400^{+1200}_{-1000}$	3040^{+140}_{-120}	$1.81^{+0.14}_{-0.16}$	$2.23^{+0.19}_{-0.18}$	$4.0^{+2.0}_{-1.4}$	$3.39^{+0.75}_{-0.49}$	$1.6^{+1.0}_{-0.7}$	
VOS 703	F1–F6	6750^{+500}_{-500}	1201^{+28}_{-27}	$1.48^{+0.26}_{-0.31}$	$1.39^{+0.13}_{-0.13}$	$3.6^{+1.3}_{-0.9}$	$2.25^{+0.50}_{-0.34}$	$3.9^{+2.4}_{-1.8}$	
VOS 738	B7	$14,000^{+500}_{-1500}$	1937^{+48}_{-46}	$2.590^{+0.035}_{-0.071}$	$2.81^{+0.07}_{-0.16}$	$4.3^{+1.6}_{-1.0}$	$4.63^{+0.46}_{-0.49}$	$0.75^{+0.30}_{-0.21}$	
VOS 759	A8	7500^{+500}_{-500}	$803.3^{+6.7}_{-6.6}$	$1.56^{+0.22}_{-0.25}$	$1.32^{+0.11}_{-0.11}$	$2.70^{+0.81}_{-0.61}$	$1.96^{+0.28}_{-0.15}$	$6.1^{+1.7}_{-2.0}$	
VOS 787	B1.5	$25,000^{+1500}_{-1500}$	3700^{+180}_{-160}	$3.33^{+0.14}_{-0.08}$	$3.89^{+0.14}_{-0.12}$	$4.7^{+1.5}_{-1.1}$	$10.9^{+1.1}_{-1.3}$	$0.104^{+0.076}_{-0.020}$	
VOS 821	F2–F8	6500^{+500}_{-500}	2098^{+53}_{-50}	$2.62^{+0.25}_{-0.26}$	$2.34^{+0.12}_{-0.12}$	$11.7^{+3.1}_{-2.9}$	$5.14^{+0.61}_{-0.70}$	$0.32^{+0.25}_{-0.12}$	Dubious/Young
VOS 854	F6–G4	6000^{+500}_{-500}	$369.7^{+2.0}_{-2.0}$	$0.82^{+0.29}_{-0.37}$	$0.13^{+0.11}_{-0.12}$	$1.07^{+0.38}_{-0.28}$	$1.08^{+0.22}_{-0.07}$	26^{+24}_{-15}	Dubious/T Tau
VOS 879	B5	$15,700^{+1000}_{-1200}$	4120^{+220}_{-200}	$2.674^{+0.033}_{-0.059}$	$3.31^{+0.12}_{-0.14}$	$6.1^{+2.2}_{-1.5}$	$6.54^{+0.87}_{-0.70}$	$0.28^{+0.12}_{-0.10}$	Dubious
VOS 898	A0	9500^{+750}_{-750}	2188^{+77}_{-72}	$2.84^{+0.12}_{-0.19}$	$2.51^{+0.14}_{-0.16}$	$6.6^{+2.6}_{-1.9}$	$4.45^{+0.81}_{-0.72}$	$0.70^{+0.53}_{-0.30}$	
VOS 911	B2–B4	$17,000^{+9000}_{-1300}$	2740^{+190}_{-170}	$2.38^{+0.43}_{-0.08}$	$3.29^{+0.63}_{-0.17}$	$5.1^{+7.3}_{-3.3}$	$6.3^{+4.8}_{-0.7}$	$0.3^{+1.2}_{-0.3}$	
VOS 934	A2	9000^{+500}_{-500}	1930^{+54}_{-51}	$2.45^{+0.13}_{-0.12}$	$2.37^{+0.11}_{-0.10}$	$6.3^{+1.7}_{-1.3}$	$4.12^{+0.57}_{-0.43}$	$0.86^{+0.36}_{-0.30}$	
VOS 941	F2–F8	6500^{+500}_{-500}	$451.0^{+7.2}_{-7.2}$	$0.37^{+0.29}_{-0.31}$	$0.28^{+0.11}_{-0.11}$	$1.09^{+0.37}_{-0.27}$	$1.21^{+0.11}_{-0.11}$	$29.0^{+9.7}_{-5.6}$	T Tau
VOS 949	A2	9000^{+500}_{-500}	2694^{+76}_{-72}	$2.37^{+0.13}_{-0.12}$	$2.58^{+0.11}_{-0.11}$	$8.0^{+2.2}_{-1.6}$	$4.91^{+0.61}_{-0.55}$	$0.50^{+0.24}_{-0.18}$	
VOS 953	G	5500^{+500}_{-500}	$444.7^{+4.1}_{-4.0}$	$1.29^{+0.34}_{-0.40}$	$0.30^{+0.12}_{-0.12}$	$1.56^{+0.61}_{-0.41}$	$1.38^{+0.28}_{-0.29}$	9^{+14}_{-7}	
VOS 983	A0	$10,000^{+1000}_{-1000}$	1543^{+38}_{-37}	$1.41^{+0.15}_{-0.22}$	$1.55^{+0.16}_{-0.18}$	$1.97^{+0.95}_{-0.65}$	$2.38^{+0.33}_{-0.30}$	5^{+25}_{-2}	
VOS 1026	B0.5	$28,000^{+3000}_{-3000}$	2773^{+77}_{-73}	$2.55^{+0.06}_{-0.15}$	$3.97^{+0.13}_{-0.18}$	$4.1^{+1.9}_{-1.4}$	$11.5^{+1.5}_{-1.7}$	$0.12^{+0.49}_{-0.05}$	
VOS 1034	B1.5–B5	$20,000^{+5000}_{-5000}$	1735^{+68}_{-63}	$5.33^{+0.23}_{-0.23}$	$3.97^{+0.33}_{-0.42}$	8^{+13}_{-5}	$10.3^{+4.5}_{-2.8}$	$0.09^{+0.61}_{-0.06}$	
VOS 1045	F1–F6	6750^{+500}_{-500}	1554^{+23}_{-23}	$1.04^{+0.27}_{-0.32}$	$1.61^{+0.12}_{-0.13}$	$4.7^{+1.6}_{-1.2}$	$2.70^{+0.56}_{-0.40}$	$2.4^{+1.5}_{-1.1}$	
VOS 1126	B2	$20,600^{+5400}_{-3600}$	3030^{+130}_{-120}	$3.37^{+0.33}_{-0.12}$	$3.66^{+0.37}_{-0.28}$	$5.3^{+6.7}_{-2.9}$	$8.1^{+3.7}_{-1.4}$	$0.18^{+0.73}_{-0.11}$	
VOS 1139	A6	8000^{+500}_{-500}	3190^{+170}_{-150}	$2.36^{+0.19}_{-0.21}$	$2.30^{+0.14}_{-0.14}$	$7.4^{+2.5}_{-1.8}$	$4.24^{+0.76}_{-0.61}$	$0.73^{+0.47}_{-0.32}$	
VOS 1152	B7	$14,000^{+500}_{-1500}$	2004^{+61}_{-58}	$2.693^{+0.035}_{-0.072}$	$2.53^{+0.08}_{-0.16}$	$3.1^{+1.2}_{-0.7}$	$3.98^{+0.37}_{-0.51}$	$1.21^{+0.51}_{-0.18}$	
VOS 1225	F1	7000^{+500}_{-500}	$456.7^{+2.8}_{-2.8}$	$0.85^{+0.25}_{-0.29}$	$0.65^{+0.11}_{-0.11}$	$1.43^{+0.45}_{-0.34}$	$1.46^{+0.15}_{-0.14}$	21^{+29}_{-9}	Dubious
VOS 1240	G9–K4	5000^{+500}_{-500}	1867^{+41}_{-39}	$2.19^{+0.35}_{-0.63}$	$2.11^{+0.12}_{-0.16}$	$15.2^{+6.3}_{-4.8}$			Cont
VOS 1245	A0	$10,000^{+1000}_{-1000}$	1664^{+49}_{-47}	$2.14^{+0.15}_{-0.21}$	$1.66^{+0.16}_{-0.19}$	$2.3^{+1.1}_{-0.8}$	$2.44^{+0.47}_{-0.32}$	4^{+24}_{-1}	
VOS 1258	B3	$17,000^{+3600}_{-300}$	4260^{+260}_{-230}	$2.42^{+0.12}_{-0.05}$	$3.16^{+0.29}_{-0.09}$	$4.4^{+2.0}_{-1.7}$	$5.7^{+1.9}_{-2.0}$	$0.4^{+3.7}_{-0.2}$	
VOS 1276	A0	$10,000^{+1000}_{-1000}$	2830^{+120}_{-113}	$0.88^{+0.15}_{-0.15}$	$2.14^{+0.17}_{-0.20}$	$3.9^{+2.0}_{-1.3}$	$3.20^{+0.71}_{-0.49}$	$1.9^{+1.1}_{-0.9}$	Dubious
VOS 1331	B0.5	$28,000^{+3000}_{-3000}$	1394^{+25}_{-25}	$6.02^{+0.08}_{-0.18}$	$3.98^{+0.13}_{-0.18}$	$4.1^{+1.9}_{-1.4}$	$11.5^{+1.5}_{-1.7}$	$0.12^{+0.49}_{-0.05}$	
VOS 1336	B2.5–B9.5	$15,000^{+5000}_{-5000}$	2246^{+61}_{-58}	$2.75^{+0.22}_{-0.39}$	$2.78^{+0.40}_{-0.55}$	$3.7^{+9.4}_{-2.6}$	$4.5^{+2.9}_{-1.3}$	$0.8^{+4.3}_{-0.7}$	
VOS 1342	B1.5–B2	$22,500^{+2500}_{-2500}$	1890^{+100}_{-90}	$5.93^{+0.13}_{-0.10}$	$4.27^{+0.19}_{-0.20}$	$9.0^{+5.2}_{-3.2}$	$12.9^{+2.5}_{-1.9}$	$0.052^{+0.032}_{-0.020}$	
VOS 1380	F2	6810^{+220}_{-90}	6900^{+850}_{-710}	$2.40^{+0.10}_{-0.04}$	$3.16^{+0.15}_{-0.11}$	$27.5^{+5.9}_{-4.8}$			Cont
VOS 1385	G0	5920^{+120}_{-40}	3950^{+480}_{-380}	$3.621^{+0.066}_{-0.029}$	$2.09^{+0.12}_{-0.10}$	$10.6^{+1.8}_{-1.5}$			Cont
VOS 1405	B1	$26,000^{+5500}_{-5400}$	5650^{+500}_{-430}	$2.31^{+0.10}_{-0.31}$	$4.12^{+0.28}_{-0.40}$	$5.6^{+6.8}_{-3.2}$	$11.8^{+4.1}_{-3.4}$	$0.08^{+0.43}_{-0.04}$	unclB[e]
VOS 1407	B9.5	$10,400^{+1200}_{-1000}$	2630^{+210}_{-180}	$3.10^{+0.14}_{-0.15}$	$2.46^{+0.22}_{-0.21}$	$5.2^{+2.9}_{-1.9}$	$4.0^{+1.1}_{-0.7}$	$0.99^{+0.83}_{-0.53}$	
VOS 1424	A7	7800^{+200}_{-300}	2870^{+300}_{-270}	$3.29^{+0.10}_{-0.10}$	$2.02^{+0.14}_{-0.13}$	$5.6^{+1.5}_{-1.0}$	$3.42^{+0.52}_{-0.38}$	$1.36^{+0.56}_{-0.48}$	
VOS 1440	B1.5	$25,000^{+5000}_{-5000}$	3280^{+280}_{-240}	$3.55^{+0.20}_{-0.21}$	$4.07^{+0.31}_{-0.36}$	$5.8^{+7.1}_{-3.1}$	$11.1^{+4.4}_{-2.7}$	$0.08^{+0.50}_{-0.05}$	unclB[e]

Table B2
(Continued)

Name	SpType	T_{eff} [K]	Distance [pc]	A_V [mag]	$\log(L [L_{\odot}])$	Radius [R_{\odot}]	Mass [M_{\odot}]	Age [Myr]	Remarks
VOS 1515	B0.5	28, 000 ⁺³⁰⁰⁰ ₋₃₀₀₀	1983 ⁺⁸⁴ ₋₇₇	6.69 ^{+0.08} _{-0.19}	4.44 ^{+0.15} _{-0.20}	7.0 ^{+3.5} _{-2.5}	14.5 ^{+3.2} _{-1.9}	0.05 ^{+0.02} _{-0.02}	
VOS 1575	B1.5–B5	20, 000 ⁺⁵⁰⁰⁰ ₋₅₀₀₀	3120 ⁺¹⁷⁰ ₋₁₆₀	5.93 ^{+0.24} _{-0.23}	4.07 ^{+0.35} _{-0.43}	9 ⁺¹⁵ ₋₆	11.1 ^{+5.3} _{-3.2}	0.07 ^{+0.15} _{-0.05}	
VOS 1600	B1.5–B2	22, 500 ⁺²⁵⁰⁰ ₋₂₅₀₀	1867 ⁺⁵⁵ ₋₅₂	4.37 ^{+0.12} _{-0.10}	4.09 ^{+0.17} _{-0.18}	7.3 ^{+3.9} _{-2.5}	11.2 ^{+1.8} _{-1.4}	0.075 ^{+0.035} _{-0.028}	
VOS 1617	B1.5	24, 800 ⁺⁴²⁰⁰ ₋₆₃₀₀	2660 ⁺¹⁰⁰ ₋₉₀	3.47 ^{+0.20} _{-0.23}	4.03 ^{+0.25} _{-0.40}	5.6 ^{+7.8} _{-3.0}	10.9 ^{+3.4} _{-3.0}	0.09 ^{+0.63} _{-0.05}	
VOS 1634	K9–M4	3500 ⁺⁵⁰⁰ ₋₅₀₀	3000 ⁺²⁷⁰ ₋₂₈₀	4.1 ^{+1.6} _{-3.6}	3.7 ^{+0.5} _{-1.0}	190 ⁺²⁶⁰ ₋₁₅₀			Cont
VOS 1635	F6–G4	6000 ⁺⁵⁰⁰ ₋₅₀₀	2340 ⁺¹¹⁰ ₋₁₀₀	2.90 ^{+0.24} _{-0.30}	2.49 ^{+0.14} _{-0.14}	16.3 ^{+6.4} _{-4.5}	5.87 ^{+0.60} _{-0.70}	0.18 ^{+0.13} _{-0.08}	Young
VOS 1672	B1.5–B2	22, 500 ⁺²⁵⁰⁰ ₋₂₅₀₀	3810 ⁺¹⁶⁰ ₋₁₅₀	3.68 ^{+0.12} _{-0.09}	4.33 ^{+0.18} _{-0.19}	9.7 ^{+5.3} _{-3.4}	13.6 ^{+2.5} _{-2.0}	0.047 ^{+0.026} _{-0.018}	
VOS 1680	A2	8840 ⁺³⁶⁰ ₋₂₉₀	3620 ⁺²⁶⁰ ₋₂₃₀	2.25 ^{+0.12} _{-0.04}	2.03 ^{+0.13} _{-0.09}	4.4 ^{+1.1} _{-0.8}	3.16 ^{+0.44} _{-0.29}	1.83 ^{+0.58} _{-0.59}	
VOS 1771	B2	22, 000 ⁺¹⁰⁰⁰ ₋₁₀₀₀	2930 ⁺¹⁰⁰ ₋₉₀	2.817 ^{+0.039} _{-0.039}	3.821 ^{+0.086} _{-0.088}	5.6 ^{+1.2} _{-1.0}	9.10 ^{+0.61} _{-0.55}	0.131 ^{+0.022} _{-0.026}	Dubious
VOS 1806	K–M	3900 ⁺¹⁴⁰⁰ ₋₁₄₀₀	2830 ⁺¹³⁰ ₋₁₂₀	2.4 ^{+1.9} _{-2.4}	2.62 ^{+0.48} _{-0.61}	45 ⁺¹⁴⁵ ₋₃₃			Cont
VOS 1873	B	21, 000 ^{+10,000} _{-10,000}	3220 ⁺²⁰⁰ ₋₁₈₀	3.50 ^{+0.41} _{-0.50}	3.86 ^{+0.56} _{-0.89}	6 ⁺³⁸ ₋₅	9 ⁺¹⁰ ₋₄	0.11 ^{+0.71} _{-0.10}	
VOS 1913	B0	31, 500 ⁺²⁵⁰⁰ ₋₅₅₀₀	3480 ⁺¹⁵⁰ ₋₁₄₀	4.28 ^{+0.06} _{-0.11}	4.77 ^{+0.12} _{-0.25}	8.2 ^{+5.6} _{-2.9}	20.1 ^{+3.3} _{-5.9}	0.03 ^{+0.16} _{-0.01}	Dubious
VOS 1922	B1.5–B5	20, 000 ⁺⁵⁰⁰⁰ ₋₅₀₀₀	3580 ⁺²¹⁰ ₋₁₈₀	5.57 ^{+0.23} _{-0.23}	4.77 ^{+0.35} _{-0.43}	20 ⁺³⁴ ₋₁₂	21 ⁺¹² ₋₇	0.02 ^{+0.09} _{-0.01}	Dubious
VOS 2047	B9.5	10, 400 ⁺¹²⁰⁰ ₋₁₀₀₀	3080 ⁺²⁰⁰ ₋₁₈₀	2.56 ^{+0.14} _{-0.16}	2.72 ^{+0.20} _{-0.19}	7.0 ^{+3.8} _{-2.5}	5.0 ^{+1.3} _{-0.9}	0.53 ^{+0.48} _{-0.29}	
VOS 2051	B1	26, 000 ⁺⁵⁵⁰⁰ ₋₅₄₀₀	3760 ⁺²⁵⁰ ₋₂₂₀	3.79 ^{+0.11} _{-0.33}	4.00 ^{+0.27} _{-0.39}	4.9 ^{+5.7} _{-2.8}	11.8 ^{+2.9} _{-3.9}	0.09 ^{+0.51} _{-0.04}	Dubious
VOS 2060	B5	15, 700 ⁺¹⁰⁰⁰ ₋₁₃₀₀	4140 ⁺²³⁰ ₋₂₀₀	2.796 ^{+0.033} _{-0.039}	3.82 ^{+0.12} _{-0.14}	11.0 ^{+3.9} _{-2.7}	9.8 ^{+1.3} _{-1.2}	0.083 ^{+0.045} _{-0.026}	Dubious
VOS 2085	B1.5	24, 800 ⁺⁴²⁰⁰ ₋₆₃₀₀	2880 ⁺²⁰⁰ ₋₁₈₀	2.66 ^{+0.19} _{-0.23}	4.15 ^{+0.28} _{-0.42}	6.4 ^{+9.4} _{-3.5}	11.7 ^{+3.6} _{-3.2}	0.07 ^{+0.42} _{-0.04}	
VOS 2093	B5	15, 700 ⁺¹⁰⁰⁰ ₋₁₂₀₀	3360 ⁺²⁴⁰ ₋₂₁₀	5.086 ^{+0.035} _{-0.062}	4.13 ^{+0.14} _{-0.15}	15.7 ^{+5.9} _{-4.1}	12.6 ^{+2.0} _{-1.8}	0.042 ^{+0.023} _{-0.014}	
VOS 2098	B7	14, 000 ⁺⁵⁰⁰ ₋₁₅₀₀	2410 ⁺⁹² ₋₈₆	3.524 ^{+0.035} _{-0.072}	3.56 ^{+0.08} _{-0.17}	10.2 ^{+3.9} _{-2.4}	8.3 ^{+1.0} _{-1.1}	0.127 ^{+0.073} _{-0.042}	
VOS 2158	B	21, 000 ^{+10,000} _{-10,000}	6520 ⁺⁹¹⁰ ₋₇₅₀	3.86 ^{+0.42} _{-0.50}	4.92 ^{+0.62} _{-0.94}	22 ⁺⁶⁰ ₋₁₄	24 ⁺²⁴ ₋₁₄	0.01 ^{+0.08} _{-0.01}	unclB[e]
VOS 2161	B2.5–B9.5	15, 000 ⁺⁵⁰⁰⁰ ₋₅₀₀₀	4560 ⁺³⁴⁰ ₋₂₉₀	3.97 ^{+0.22} _{-0.40}	3.80 ^{+0.45} _{-0.59}	12 ⁺³³ ₋₈	9.8 ^{+7.2} _{-3.8}	0.08 ^{+0.31} _{-0.07}	unclB[e]
VOS 2164			3610 ⁺²⁹⁰ ₋₂₅₀						Cont
VOS 2169	B1.5–B5	20, 000 ⁺⁵⁰⁰⁰ ₋₅₀₀₀	4530 ⁺²⁴⁰ ₋₂₂₀	2.84 ^{+0.21} _{-0.22}	4.03 ^{+0.34} _{-0.42}	9 ⁺¹⁴ ₋₅	10.8 ^{+4.9} _{-3.0}	0.08 ^{+0.62} _{-0.05}	
VOS 2171	B	21, 000 ^{+10,000} _{-10,000}	5140 ⁺³⁹⁰ ₋₃₄₀	4.41 ^{+0.43} _{-0.51}	4.21 ^{+0.57} _{-0.90}	10 ⁺⁵⁹ ₋₈	12 ⁺¹⁴ ₋₆	0.05 ^{+0.31} _{-0.05}	
VOS 2196	B1.5–B2	22, 500 ⁺²⁰⁰⁰ ₋₂₀₀₀	2680 ⁺¹²⁰ ₋₁₁₀	2.185 ^{+0.077} _{-0.075}	3.54 ^{+0.15} _{-0.16}	3.9 ^{+1.6} _{-1.1}	8.3 ^{+1.1} _{-1.0}	0.21 ^{+0.69} _{-0.07}	
VOS 3851	G	5500 ⁺⁵⁰⁰ ₋₅₀₀	408.7 ^{+4.2} _{-4.1}	0.71 ^{+0.36} _{-0.42}	-0.06 ^{+0.12} _{-0.12}	1.03 ^{+0.41} _{-0.28}	1.00 ^{+0.28} _{-0.08}	25 ⁺²⁵ ₋₁₇	T Tau
VOS 4439	K5	4500 ⁺⁵⁰⁰ ₋₅₀₀	240 ⁺¹³ ₋₁₂	1.5 ^{+0.6} _{-1.0}	-0.07 ^{+0.19} _{-0.27}	1.52 ^{+0.88} _{-0.62}	1.04 ^{+0.30} _{-0.46}	4 ⁺²⁴ ₋₃	T Tau
VOS 4463	K5	4500 ⁺⁵⁰⁰ ₋₅₀₀	200.76 ^{+0.74} _{-0.73}	0.12 ^{+0.72} _{-0.12}	-0.51 ^{+0.17} _{-0.09}	0.91 ^{+0.49} _{-0.17}	0.87 ^{+0.11} _{-0.15}	19 ⁺²⁷ ₋₁₆	T Tau
VOS 4614	K5	4500 ⁺⁵⁰⁰ ₋₅₀₀	184.31 ^{+0.49} _{-0.48}	1.9 ^{+0.6} _{-1.0}	0.00 ^{+0.14} _{-0.22}	1.65 ^{+0.81} _{-0.62}	1.00 ^{+0.36} _{-0.43}	3 ⁺¹⁶ ₋₂	T Tau

Note. Effective temperatures (T_{eff}) or spectral types derived from spectra (Section 2.1) appear in boldface type. T_{eff} values or spectral types not in boldface were approximated from the spectral derivations using the conversions of Pecaut & Mamajek (2013). See Section 3 for a description on the derivation of the stellar parameters, distances, and extinctions. Stellar radii were derived following Equation (2). VOS 1617 was observed with both IDS and EFOSC2 settings and was assigned a B1.5 and a B3 spectral type respectively. Given the better resolution of the IDS configuration and its smaller spectral type uncertainty we consider the B1.5 spectral type determination for this object in this work. Remarks column: “Cont” indicates the non-PMS contaminants discussed in Section 4; “Dubious” marks those 13 sources described in Appendix A with no detected $H\alpha$ emission and little IR excess. These stars have a less secure YSO nature than the other sources; “unclB[e]” indicates the four sources identified as of a FS CMa (unclassified B[e]) nature (see Appendix A); “Young” shows the four sources that are younger than previously known stars of a similar mass (see Appendix A). “T Tau” indicates that the source is inconsistent with $M > 1.5 M_{\odot}$ and hence it likely belongs to the T Tauri regime. (This table is available in its entirety in machine-readable form.)

Table B3
 $H\alpha$ and $H\beta$ Observed Equivalent Widths (EW_{obs}) and Line Profiles, and the derived Accretion Rates and IR Excesses

Name	$H\alpha$ EW_{obs} [Å]	$H\beta$ EW_{obs} [Å]	EW_{corr} [Å]	Line Profile	\dot{M}_{acc} [$M_{\odot}\text{yr}^{-1}$]	L_{IR}/L_{*}	Remarks
VOS 4	-3.30		-13.00	d	$(0.55_{-0.20}^{+0.31}) \cdot 10^{-7}$	$0.316_{-0.054}^{+0.067}$	
VOS 7						$0.39_{-0.10}^{+0.13}$	
VOS 15	-8.70		-17.75	d	$(1.05_{-0.46}^{+0.74}) \cdot 10^{-7}$	$0.58_{-0.13}^{+0.17}$	
VOS 20	3.23		-4.98	iP	$(2.02_{-0.55}^{+0.71}) \cdot 10^{-8}$	$0.212_{-0.011}^{+0.031}$	
VOS 22	-53.98		-60.42	d	$(0.11_{-0.08}^{+0.25}) \cdot 10^{-4}$	$0.27_{-0.12}^{+0.28}$	
VOS 24	0.26		-2.66	d	$(1.30_{-0.31}^{+0.46}) \cdot 10^{-8}$	$0.255_{-0.031}^{+0.025}$	
VOS 26	-23.50		-34.03	d	$(0.16_{-0.09}^{+0.22}) \cdot 10^{-5}$	$0.42_{-0.14}^{+0.24}$	
VOS 32	0.36		-2.56	rP	$(2.36_{-0.60}^{+0.88}) \cdot 10^{-8}$	$0.586_{-0.047}^{+0.030}$	
VOS 35						$0.24_{-0.16}^{+0.18}$	
VOS 42	-123.00		-126.70	s	$(0.02_{-0.02}^{+0.29}) \cdot 10^{-4}$	$0.02_{-0.01}^{+0.10}$	
VOS 48	-4.49		-7.41	d	$(0.36_{-0.09}^{+0.13}) \cdot 10^{-7}$	$0.246_{-0.033}^{+0.027}$	
VOS 50		-14.32	-15.37	s	$(0.18_{-0.11}^{+0.36}) \cdot 10^{-8}$	$0.45_{-0.42}^{+0.85}$	T Tau
VOS 51	-4.77		-10.41	d	$(0.95_{-0.35}^{+0.79}) \cdot 10^{-7}$	$0.054_{-0.007}^{+0.022}$	
VOS 55	-17.00		-18.01	s	$(0.13_{-0.08}^{+0.32}) \cdot 10^{-6}$	$0.62_{-0.33}^{+0.56}$	
VOS 56	-3.04		-12.51	d	$(1.37_{-0.43}^{+0.59}) \cdot 10^{-7}$	$0.294_{-0.049}^{+0.035}$	
VOS 63	-0.32		-8.24	d	$(0.22_{-0.07}^{+0.10}) \cdot 10^{-5}$	$0.095_{-0.017}^{+0.018}$	Young
VOS 67	-1.96		-4.88	rP	$(2.77_{-0.73}^{+0.95}) \cdot 10^{-6}$	$0.091_{-0.018}^{+0.017}$	Young
VOS 69	-8.17		-17.87	d	$(0.65_{-0.26}^{+0.37}) \cdot 10^{-7}$	$0.52_{-0.10}^{+0.15}$	
VOS 70	2.29		-6.41	iP	$(0.71_{-0.23}^{+0.37}) \cdot 10^{-6}$	$0.099_{-0.016}^{+0.017*}$	
VOS 76	2.45		-6.03	s	$(0.19_{-0.09}^{+0.16}) \cdot 10^{-6}$	$1.20_{-0.27}^{+0.36*}$	
VOS 77						$0.34_{-0.25}^{+0.41}$	
VOS 78	-5.66		-13.87	d	$(1.45_{-0.46}^{+0.72}) \cdot 10^{-7}$	$0.90_{-0.05}^{+0.13*}$	
VOS 84						$0.287_{-0.069}^{+0.092}$	
VOS 95	-3.60		-14.29	d	$(0.26_{-0.10}^{+0.15}) \cdot 10^{-6}$	$0.166_{-0.031}^{+0.046}$	
VOS 104	2.06		-7.94	d	$(0.56_{-0.18}^{+0.25}) \cdot 10^{-7}$	$0.126_{-0.025}^{+0.016}$	
VOS 105	0.33		-4.74	iP	$(1.51_{-0.47}^{+0.73}) \cdot 10^{-7}$	$0.177_{-0.025}^{+0.032*}$	
VOS 108	-32.00		-42.69	d	$(0.19_{-0.08}^{+0.14}) \cdot 10^{-5}$	$0.43_{-0.08}^{+0.12}$	
VOS 111	-24.77		-35.31	d	$(0.13_{-0.06}^{+0.11}) \cdot 10^{-5}$	$0.184_{-0.059}^{+0.046}$	
VOS 112	2.00		-0.23	iP	$(0.23_{-0.11}^{+0.26}) \cdot 10^{-7}$	$0.15_{-0.13}^{+0.13}$	
VOS 118						$0.14_{-0.11}^{+0.11*}$	
VOS 121	0.85		-8.12	d	$(0.39_{-0.20}^{+0.35}) \cdot 10^{-7}$	$0.111_{-0.035}^{+0.049}$	
VOS 125	-55.42		-59.45	s	$(0.15_{-0.10}^{+0.26}) \cdot 10^{-4}$	$0.055_{-0.019}^{+0.037}$	
VOS 131	-0.20		-3.86	d	$(0.17_{-0.09}^{+0.17}) \cdot 10^{-7}$	$0.20_{-0.10}^{+0.11}$	
VOS 135	-1.86		-4.78	d	$(0.25_{-0.08}^{+0.13}) \cdot 10^{-6}$	$0.272_{-0.032}^{+0.025}$	
VOS 136	-7.90		-10.52	d	$(0.26_{-0.13}^{+0.27}) \cdot 10^{-7}$	$0.24_{-0.13}^{+0.13}$	
VOS 140	-13.63		-22.60	d	$(0.14_{-0.08}^{+0.16}) \cdot 10^{-6}$	$0.22_{-0.07}^{+0.10}$	
VOS 164	1.61		-7.09	d	$(0.50_{-0.17}^{+0.26}) \cdot 10^{-7}$	$0.187_{-0.029}^{+0.033}$	
VOS 184	-49.66		-60.20	d	$(0.16_{-0.08}^{+0.14}) \cdot 10^{-5}$	$0.266_{-0.082}^{+0.064}$	
VOS 199						$0.36_{-0.09}^{+0.13}$	
VOS 200		-2.69	-15.10	s	$(0.42_{-0.26}^{+0.66}) \cdot 10^{-4}$	$0.33_{-0.10}^{+0.17}$	
VOS 209	2.50			abs		$0.076_{-0.044}^{+0.055}$	T Tau
VOS 215	6.90		-4.70	d	$(0.41_{-0.15}^{+0.25}) \cdot 10^{-7}$	$0.138_{-0.023}^{+0.030}$	
VOS 224	-13.00		-28.00	s	$(0.46_{-0.18}^{+0.25}) \cdot 10^{-6}$	$0.173_{-0.031}^{+0.039}$	
VOS 233	-2.85		-11.90	d	$(0.28_{-0.13}^{+0.24}) \cdot 10^{-6}$	$0.51_{-0.12}^{+0.16}$	
VOS 247	-2.88		-11.85	d	$(0.55_{-0.30}^{+0.59}) \cdot 10^{-6}$	$0.130_{-0.040}^{+0.056}$	
VOS 250						$0.193_{-0.038}^{+0.061}$	
VOS 253	-6.10		-18.80	s	$(1.00_{-0.40}^{+0.55}) \cdot 10^{-7}$	$0.238_{-0.042}^{+0.062}$	
VOS 271		-2.50	-17.34	s	$(0.34_{-0.17}^{+0.33}) \cdot 10^{-5}$	$0.52_{-0.10}^{+0.15}$	
VOS 274		9.13	-5.71	s	$(0.82_{-0.34}^{+0.66}) \cdot 10^{-7}$	$0.42_{-0.08}^{+0.12}$	
VOS 284	2.90		-5.95	d	$(0.89_{-0.38}^{+0.64}) \cdot 10^{-7}$	$0.215_{-0.054}^{+0.061}$	
VOS 290	-63.00		-66.75	rP	$(0.12_{-0.09}^{+0.29}) \cdot 10^{-4}$	$0.070_{-0.039}^{+0.057}$	
VOS 293	-20.10		-27.25	d	$(0.50_{-0.24}^{+0.43}) \cdot 10^{-6}$	$0.085_{-0.019}^{+0.026}$	
VOS 297						$0.33_{-0.08}^{+0.11}$	
VOS 321						$0.33_{-0.08}^{+0.11}$	
VOS 336						$0.19_{-0.09}^{+0.10}$	
VOS 341	-48.00		-57.70	s	$(0.67_{-0.36}^{+0.72}) \cdot 10^{-6}$	$0.20_{-0.06}^{+0.11}$	
VOS 361	4.70		-3.78	iP	$(0.34_{-0.15}^{+0.23}) \cdot 10^{-7}$	$0.233_{-0.057}^{+0.077}$	
VOS 373	7.20		-2.50	d	$(0.94_{-0.40}^{+0.70}) \cdot 10^{-7}$	$0.243_{-0.048}^{+0.076}$	

Table B3
(Continued)

Name	H α EW _{obs} [Å]	H β EW _{obs} [Å]	EW _{corr} [Å]	Line Profile	M' acc [$M_{\odot}\text{yr}^{-1}$]	L_{IR}/L_{*}	Remarks
VOS 398						$0.06^{+0.12}_{-0.06}$	
VOS 406	-39.00		-39.54	s	$(0.19^{+0.44}_{-0.11}) \cdot 10^{-7}$	$0.16^{+0.16}_{-0.16}$	T Tau
VOS 413	-35.00		-43.00	s	$(0.97^{+0.84}_{-0.49}) \cdot 10^{-6}$	$0.134^{+0.056}_{-0.032}$	
VOS 431						$0.176^{+0.060}_{-0.045}$	
VOS 445	-31.00		-39.00	s	$(0.71^{+0.82}_{-0.38}) \cdot 10^{-5}$	$0.171^{+0.070}_{-0.040}$	
VOS 448	2.20			abs		$(0.00^{+0.62}_{-0.00}) \cdot 10^{-3*}$	Dubious
VOS 458	-2.90		-5.50	rP		$0.17^{+0.12}_{-0.13}$	Cont
VOS 461	-57.00		-66.70	rP	$(0.13^{+0.13}_{-0.07}) \cdot 10^{-5}$	$0.30^{+0.15}_{-0.09}$	
VOS 465	6.40		-2.45	s	$(0.16^{+0.10}_{-0.06}) \cdot 10^{-7}$	$0.184^{+0.052}_{-0.046}$	
VOS 473		12.18	-0.23	s	$(0.18^{+0.19}_{-0.10}) \cdot 10^{-8}$	$0.19^{+0.10}_{-0.06}$	
VOS 475	-0.58		-9.55	s	$(0.50^{+0.63}_{-0.29}) \cdot 10^{-6}$	$0.140^{+0.061}_{-0.044}$	
VOS 476	-27.00		-35.00	rP	$(0.06^{+0.12}_{-0.04}) \cdot 10^{-5}$	$0.15^{+0.16}_{-0.06}$	
VOS 481		-5.06	-8.27	s	$(0.23^{+0.21}_{-0.13}) \cdot 10^{-7}$	$0.18^{+0.10}_{-0.09}$	
VOS 482	-53.00		-63.69	s	$(0.54^{+0.38}_{-0.23}) \cdot 10^{-6}$	$0.39^{+0.10}_{-0.07}$	
VOS 491	11.20			abs		>5*	Dubious
VOS 495	3.24			abs		$(0.00^{+0.74}_{-0.00}) \cdot 10^{-3}$	Dubious
VOS 519	0.00		-11.00	s	$(0.54^{+0.41}_{-0.24}) \cdot 10^{-7}$	$0.60^{+0.16}_{-0.14}$	
VOS 522						$0.34^{+0.11}_{-0.08}$	
VOS 588	-54.41		-60.85	rP	$(0.06^{+0.10}_{-0.04}) \cdot 10^{-4}$	$0.18^{+0.10}_{-0.05}$	
VOS 595		-1.20	-11.70	s	$(0.8^{+1.2}_{-0.5}) \cdot 10^{-5}$	$0.24^{+0.10}_{-0.06}$	
VOS 603		-2.51		s			Cont
VOS 668	10.40			abs		$0.061^{+0.016*}_{-0.012}$	
VOS 672	-76.36		-80.26	s	$(0.03^{+0.22}_{-0.02}) \cdot 10^{-3}$	$0.06^{+0.21*}_{-0.04}$	
VOS 689	3.60		-5.37	d	$(0.26^{+0.31}_{-0.15}) \cdot 10^{-6}$	$0.062^{+0.029}_{-0.020}$	
VOS 703	0.10		-6.07	d	$(1.01^{+0.91}_{-0.50}) \cdot 10^{-7}$	$0.112^{+0.062}_{-0.060}$	
VOS 738	-0.81		-6.45	s	$(0.46^{+0.39}_{-0.19}) \cdot 10^{-6}$	$0.031^{+0.013}_{-0.004}$	
VOS 759		10.11	-4.39	s	$(1.13^{+0.87}_{-0.52}) \cdot 10^{-7}$	$0.133^{+0.047*}_{-0.039}$	
VOS 787		1.83	-0.46	s	$(0.24^{+0.26}_{-0.12}) \cdot 10^{-6}$	$(0.61^{+0.36}_{-0.45}) \cdot 10^{-3}$	
VOS 821						$0.014^{+0.047*}_{-0.014}$	Dubious/Young
VOS 854	2.87			abs		$0.48^{+0.19}_{-0.14}$	Dubious/T Tau
VOS 879						$(0.59^{+0.21}_{-0.13}) \cdot 10^{-2}$	Dubious
VOS 898		7.68	-6.17	s	$(0.52^{+0.63}_{-0.28}) \cdot 10^{-5}$	$0.201^{+0.081}_{-0.050}$	
VOS 911	-5.50		-9.66	d	$(0.11^{+0.29}_{-0.09}) \cdot 10^{-5}$	$(0.28^{+0.16}_{-0.28}) \cdot 10^{-2}$	
VOS 934						$0.050^{+0.015}_{-0.013}$	
VOS 941	3.60		-1.49	s	$(1.12^{+0.80}_{-0.45}) \cdot 10^{-9}$	$0.162^{+0.074}_{-0.075}$	T Tau
VOS 949						$0.043^{+0.013}_{-0.012}$	
VOS 953	-6.40		-8.49	d	$(0.87^{+0.91}_{-0.41}) \cdot 10^{-8}$	$0.08^{+0.13}_{-0.08}$	
VOS 983	-70.00		-79.70	s	$(0.59^{+0.61}_{-0.30}) \cdot 10^{-6}$	$0.64^{+0.31}_{-0.18}$	
VOS 1026	3.05		-0.15	s	$(0.12^{+0.13}_{-0.06}) \cdot 10^{-7}$	$(0.73^{+0.62}_{-0.23}) \cdot 10^{-3*}$	
VOS 1034	-79.78		-83.58	d	$(0.03^{+0.10}_{-0.02}) \cdot 10^{-3}$	$(0.22^{+0.42}_{-0.17}) \cdot 10^{-2}$	
VOS 1045						$0.036^{+0.051*}_{-0.036}$	
VOS 1126		-0.31	-2.60	s	$(0.27^{+0.73}_{-0.20}) \cdot 10^{-5}$	$(0.61^{+0.52}_{-0.38}) \cdot 10^{-2}$	
VOS 1139						$0.258^{+0.079}_{-0.061}$	
VOS 1152	-34.92		-40.56	s	$(0.13^{+0.12}_{-0.05}) \cdot 10^{-5}$	$0.085^{+0.035}_{-0.011}$	
VOS 1225						$0.026^{+0.040*}_{-0.026}$	Dubious
VOS 1240						$5.0^{+4.0*}_{-1.9}$	Cont
VOS 1245	-1.60		-14.00	s	$(0.15^{+0.16}_{-0.08}) \cdot 10^{-6}$	$0.175^{+0.089}_{-0.051}$	
VOS 1258	-67.00		-71.16	s	$(0.58^{+0.56}_{-0.37}) \cdot 10^{-5}$	$(0.40^{+0.11}_{-0.20}) \cdot 10^{-2}$	
VOS 1276						$0.010^{+0.010}_{-0.009}$	Dubious
VOS 1331	-267.40		-270.60	s	$(0.21^{+0.22}_{-0.11}) \cdot 10^{-4}$	$(1.55^{+0.92}_{-0.44}) \cdot 10^{-2}$	
VOS 1336	-231.00		-236.07	d	$(0.12^{+0.60}_{-0.10}) \cdot 10^{-4}$	$0.06^{+0.16*}_{-0.04}$	
VOS 1342	-377.70		-381.30	s	$(0.18^{+0.25}_{-0.11}) \cdot 10^{-3}$	$0.041^{+0.029}_{-0.016}$	
VOS 1380	-1.28		-7.58	d		$0.197^{+0.014}_{-0.028}$	Cont
VOS 1385	-1.72		-4.64	s		$2.51^{+0.11*}_{-0.19}$	Cont
VOS 1405	-60.00		-63.30	s	$(0.11^{+0.34}_{-0.08}) \cdot 10^{-4}$	$0.022^{+0.026}_{-0.008}$	unclB[e]
VOS 1407	-12.55		-21.52	d	$(0.19^{+0.29}_{-0.12}) \cdot 10^{-5}$	$0.187^{+0.081}_{-0.058}$	
VOS 1424	-8.88		-17.58	d	$(0.12^{+0.12}_{-0.06}) \cdot 10^{-5}$	$0.439^{+0.070}_{-0.062}$	
VOS 1440	-19.06		-22.46	s	$(0.04^{+0.12}_{-0.03}) \cdot 10^{-4}$	$0.030^{+0.031}_{-0.013}$	unclB[e]

Table B3
(Continued)

Name	H α EW _{obs} [Å]	H β EW _{obs} [Å]	EW _{corr} [Å]	Line Profile	M _{acc} [$M_{\odot}\text{yr}^{-1}$]	L_{IR}/L_{*}	Remarks
VOS 1515	-76.21		-79.41	s	$(0.24^{+0.28}_{-0.14}) \cdot 10^{-4}$	$(0.81^{+0.77}_{-0.28}) \cdot 10^{-3}$	
VOS 1575	-45.78		-49.58	s	$(0.23^{+0.87}_{-0.18}) \cdot 10^{-4}$	$(0.22^{+0.42}_{-0.17}) \cdot 10^{-2}$	
VOS 1600	-19.28		-22.88	s	$(0.69^{+0.79}_{-0.37}) \cdot 10^{-5}$	$(0.22^{+0.13}_{-0.09}) \cdot 10^{-2*}$	
VOS 1617	-25.25		-28.65	s	$(0.05^{+0.15}_{-0.03}) \cdot 10^{-4}$	$(0.09^{+0.19}_{-0.09}) \cdot 10^{-2*}$	
VOS 1634						$0.0^{+1.5*}_{-0.0}$	Cont
VOS 1635	-18.50		-22.16	d	$(0.85^{+0.85}_{-0.40}) \cdot 10^{-5}$	$0.08^{+0.077}_{-0.079}$	Young
VOS 1672	-34.19		-37.79	d	$(0.22^{+0.27}_{-0.12}) \cdot 10^{-4}$	$(0.18^{+0.10}_{-0.07}) \cdot 10^{-2}$	
VOS 1680	-69.68		-79.68	d	$(0.38^{+0.31}_{-0.17}) \cdot 10^{-5}$	$0.207^{+0.023}_{-0.037}$	
VOS 1771						$(0.70^{+0.13}_{-0.11}) \cdot 10^{-2*}$	Dubious
VOS 1806						$0.1^{+1.4*}_{-0.1}$	Cont
VOS 1873	-8.31		-12.01	d	$(0.03^{+0.41}_{-0.02}) \cdot 10^{-4}$	$0.008^{+0.048}_{-0.006}$	
VOS 1913						$(0.69^{+0.57}_{-0.20}) \cdot 10^{-3}$	Dubious
VOS 1922	1.38			abs		$(0.00^{+0.11}_{-0.00}) \cdot 10^{-2*}$	Dubious
VOS 2047	-7.05		-16.02	s	$(0.28^{+0.40}_{-0.17}) \cdot 10^{-5}$	$0.036^{+0.018}_{-0.012}$	
VOS 2051						$(0.07^{+0.17}_{-0.05}) \cdot 10^{-2*}$	Dubious
VOS 2060	3.50			abs		$(0.00^{+0.90}_{-0.00}) \cdot 10^{-3*}$	Dubious
VOS 2085	3.09		-0.31	s	$(0.07^{+0.25}_{-0.05}) \cdot 10^{-6}$	$0.007^{+0.010*}_{-0.003}$	
VOS 2093	-59.00		-63.73	s	$(0.10^{+0.11}_{-0.05}) \cdot 10^{-3}$	$(0.43^{+0.18}_{-0.10}) \cdot 10^{-2*}$	
VOS 2098	-16.31		-21.95	s	$(0.12^{+0.11}_{-0.05}) \cdot 10^{-4}$	$0.026^{+0.011}_{-0.004}$	
VOS 2158	-1257.00		-1260.70	d	$0.004^{+0.106}_{-0.004}$	$0.12^{+0.83}_{-0.09}$	unclB[e]
VOS 2161	-175.00		-180.07	s	$(0.01^{+0.10}_{-0.01}) \cdot 10^{-2}$	$1.1^{+3.0*}_{-0.7}$	unclB[e]
VOS 2164							Cont
VOS 2169	-157.70		-161.50	s	$(0.07^{+0.25}_{-0.05}) \cdot 10^{-3}$	$0.038^{+0.055}_{-0.019}$	
VOS 2171	-168.50		-172.20	d	$(0.01^{+0.17}_{-0.01}) \cdot 10^{-2}$	$0.04^{+0.26}_{-0.03}$	
VOS 2196		-12.57	-14.86	s	$(0.9^{+1.1}_{-0.5}) \cdot 10^{-5}$	$0.060^{+0.022}_{-0.015}$	
VOS 3851	-0.50		-2.59	d	$(1.04^{+0.81}_{-0.53}) \cdot 10^{-9}$	$0.41^{+0.25*}_{-0.21}$	T Tau
VOS 4439	-11.60		-12.30	d	$(0.06^{+0.15}_{-0.04}) \cdot 10^{-7}$	$0.09^{+0.54}_{-0.09}$	T Tau
VOS 4463						$0.09^{+0.15}_{-0.09}$	T Tau
VOS 4614	-16.50		-17.20	s	$(0.11^{+0.22}_{-0.07}) \cdot 10^{-7}$	$0.17^{+0.59}_{-0.17}$	T Tau

Note. EW_{corr} refers to the values which result from correcting EW_{obs} from the typical line absorption EW of each spectral type (Section 5). See Section 5 for a description on the derivation of the accretion rates. The amount of IR excess is shown in column L_{IR}/L_{*} (Section 3.2). H β EW_{obs} values and H β line profiles are only presented when H β has emission and H α was not observed. Boldface type indicates that a value was derived from the H β line and not from the H α line. The line profiles are “s” for single-peaked emission, “d” for double-peaked, “rP” for regular P-Cygni, and “iP” for inverse P-Cygni. L_{IR}/L_{*} values marked with an asterisk likely have contamination from extended background emission (Section 3.2). Remarks column: “Cont” indicates the non-PMS contaminants discussed in Section 4; “Dubious” marks those 13 sources described in Appendix A with no detected H α emission and little IR excess; these stars have a less secure YSO nature than the other sources; “unclB[e]” indicates the four sources identified as of a FS CMA (unclassified B[e]) nature (see Appendix A); “Young” shows the four sources that are younger than previously known stars of a similar mass (see Appendix A); “T Tau” indicates that the source is inconsistent with $M > 1.5 M_{\odot}$ and hence it likely belongs to the T Tauri regime.

(This table is available in its entirety in machine-readable form.)

ORCID iDs

Miguel Vioque  <https://orcid.org/0000-0002-4147-3846>
René D. Oudmaijer  <https://orcid.org/0000-0001-7703-3992>
Ignacio Mendigutía  <https://orcid.org/0000-0002-0233-5328>
Deborah Baines  <https://orcid.org/0000-0002-6923-3756>
Olja Panić  <https://orcid.org/0000-0002-6648-2968>
Daniela Iglesias  <https://orcid.org/0000-0002-0756-9836>
James Miley  <https://orcid.org/0000-0002-1575-680X>
Ricardo Pérez-Martínez  <https://orcid.org/0000-0002-9127-5522>

References

- Ababakr, K. M., Fairlamb, J. R., Oudmaijer, R. D., & van den Ancker, M. E. 2015, *MNRAS*, 452, 2566
- Ababakr, K. M., Oudmaijer, R. D., & Vink, J. S. 2017, *MNRAS*, 472, 854
- Andrews, S. M., Rosenfeld, K. A., Kraus, A. L., & Wilner, D. J. 2013, *ApJ*, 771, 129
- Ansdell, M., Williams, J. P., van der Marel, N., et al. 2016, *ApJ*, 828, 46
- Bailer-Jones, C. A. L., Rybizki, J., Fouesneau, M., Demleitner, M., & Andrae, R. 2021, *AJ*, 161, 147
- Banzatti, A., Garufi, A., Kama, M., et al. 2018, *A&A*, 609, L2
- Bohlin, R. C., Mészáros, S., Fleming, S. W., et al. 2017, *AJ*, 153, 234
- Bouvier, J., Alencar, S. H. P., Harries, T. J., Johns-Krull, C. M., & Romanova, M. M. 2007, in *Protostars and Planets V*, ed. B. Reipurth, D. Jewitt, & K. Keil (Tucson, AZ: Univ. Arizona Press), 479
- Bouvier, J., Perraut, K., Le Bouquin, J. B., et al. 2020, *A&A*, 636, A108
- Braga, V. F., Bhardwaj, A., Contreras Ramos, R., et al. 2018, *A&A*, 619, A51
- Bressan, A., Marigo, P., Girardi, L., et al. 2012, *MNRAS*, 427, 127
- Calvet, N., Muzerolle, J., Briceño, C., et al. 2004, *AJ*, 128, 1294
- Casagrande, L., Lin, J., Rains, A. D., et al. 2021, *MNRAS*, 507, 2684
- Castelli, F., & Kurucz, R. L. 2003, in *IAU Symp. 210, Modelling of Stellar Atmospheres*, ed. N. Piskunov, W. W. Weiss, & D. F. Gray (Cambridge: Cambridge Univ. Press), A20
- Cieza, L. A., González-Ruilova, C., Hales, A. S., et al. 2021, *MNRAS*, 501, 2934
- Cutri, R. M., Wright, E. L., Conrow, T., et al. 2013, *Explanatory Supplement to the AllWISE Data Release Products*, Tech. Rep., <https://wise2.ipac.caltech.edu/docs/release/allwise/expsup/index.html>

- Fairlamb, J. R., Oudmaijer, R. D., Mendigutía, I., Ilee, J. D., & van den Ancker, M. E. 2015, *MNRAS*, **453**, 976
- Fairlamb, J. R., Oudmaijer, R. D., Mendigutía, I., Ilee, J. D., & van den Ancker, M. E. 2017, *MNRAS*, **464**, 4721
- Frost, A. J., Oudmaijer, R. D., de Wit, W. J., & Lumsden, S. L. 2021, *A&A*, **648**, A62
- Gaia Collaboration, Prusti, T., de Bruijne, J. H. J., et al. 2016, *A&A*, **595**, A1
- Gaia Collaboration, Brown, A. G. A., Vallenari, A., et al. 2021, *A&A*, **649**, A1
- Garufi, A., Benisty, M., Pinilla, P., et al. 2018, *A&A*, **620**, A94
- Grant, S. L., Espaillat, C. C., Brittain, S., Scott-Joseph, C., & Calvet, N. 2022, *ApJ*, **926**, 229
- Gravity Collaboration, Garcia Lopez, R., Natta, A., et al. 2020, *Natur*, **584**, 547
- Groenewegen, M. A. T., Sevenster, M., Spoon, H. W. W., & Pérez, I. 2002, *A&A*, **390**, 501
- Guzmán-Díaz, J., Mendigutía, I., Montesinos, B., et al. 2021, *A&A*, **650**, A182
- Hartmann, L., Herczeg, G., & Calvet, N. 2016, *ARA&A*, **54**, 135
- Hernández, J., Calvet, N., Briceño, C., Hartmann, L., & Berlind, P. 2004, *AJ*, **127**, 1682
- Hofmann, K. H., Bensberg, A., Schertl, D., et al. 2022, *A&A*, **658**, A81
- Joner, M. D., & Hintz, E. G. 2015, *AJ*, **150**, 204
- Kaler, J. B., Aller, L. H., & Czyzak, S. J. 1976, *ApJ*, **203**, 636
- Keller, L. D., Sloan, G. C., Oliveira, J. M., et al. 2019, *ApJ*, **878**, 147
- Koenig, X. P., & Leisawitz, D. T. 2014, *ApJ*, **791**, 131
- Koumpia, E., Ababakr, K. M., de Wit, W. J., et al. 2019, *A&A*, **623**, L5
- Koumpia, E., de Wit, W. J., Oudmaijer, R. D., et al. 2021, *A&A*, **654**, A109
- Kuffmeier, M., Frimann, S., Jensen, S. S., & Haugbølle, T. 2018, *MNRAS*, **475**, 2642
- Kunitomo, M., Ida, S., Takeuchi, T., et al. 2021, *ApJ*, **909**, 109
- Lamers, H. J. G. L. M., Zickgraf, F.-J., de Winter, D., Houziaux, L., & Zorec, J. 1998, *A&A*, **340**, 117
- Lindgren, L., Klioner, S. A., Hernández, J., et al. 2021a, *A&A*, **649**, A2
- Lindgren, L., Bastian, U., Biermann, M., et al. 2021b, *A&A*, **649**, A4
- Lumsden, S. L., Hoare, M. G., Urquhart, J. S., et al. 2013, *ApJS*, **208**, 11
- Marcos-Arenal, P., Mendigutía, I., Koumpia, E., et al. 2021, *A&A*, **652**, A68
- Marigo, P., Girardi, L., Bressan, A., et al. 2017, *ApJ*, **835**, 77
- Mendigutía, I. 2020, *Galax*, **8**, 39
- Mendigutía, I., Calvet, N., Montesinos, B., et al. 2011, *A&A*, **535**, A99
- Mendigutía, I., Oudmaijer, R. D., Mourard, D., & Muzerolle, J. 2017, *MNRAS*, **464**, 1984
- Mendigutía, I., Oudmaijer, R. D., Rigliaco, E., et al. 2015, *MNRAS*, **452**, 2837
- Miley, J. M., Panić, O., Booth, R. A., et al. 2021, *MNRAS*, **500**, 4658
- Miroshnichenko, A. S. 2007, *ApJ*, **667**, 497
- Monnier, J. D., Millan-Gabet, R., Billmeier, R., et al. 2005, *ApJ*, **624**, 832
- Moór, A., Abraham, P., Szabó, G., et al. 2021, *ApJ*, **910**, 27
- Natta, A., Testi, L., & Randich, S. 2006, *A&A*, **452**, 245
- Núñez, E. H., Povich, M. S., Binder, B. A., Townsley, L. K., & Broos, P. S. 2021, *AJ*, **162**, 153
- Otulakowska-Hypka, M., Olech, A., & Patterson, J. 2016, *MNRAS*, **460**, 2526
- Oudmaijer, R. D., & Miroshnichenko, A. S. 2017, in ASP Conf. Ser. 508, The B[e] Phenomenon: Forty Years of Studies, ed. A. Miroshnichenko et al. (San Francisco, CA: ASP), **3**
- Panić, O., & Min, M. 2017, *MNRAS*, **467**, 1175
- Pascual, N., Montesinos, B., Meeus, G., et al. 2016, *A&A*, **586**, A6
- Pascucci, I., Testi, L., Herczeg, G. J., et al. 2016, *ApJ*, **831**, 125
- Pecaut, M. J., & Mamajek, E. E. 2013, *ApJS*, **208**, 9
- Povich, M. S., Townsley, L. K., Robitaille, T. P., et al. 2016, *ApJ*, **825**, 125
- Reffert, S., Bergmann, C., Quirrenbach, A., Trifonov, T., & Künstler, A. 2015, *A&A*, **574**, A116
- Ribas, Á., Merín, B., Bouy, H., & Maud, L. T. 2014, *A&A*, **561**, A54
- Riello, M., De Angeli, F., Evans, D. W., et al. 2021, *A&A*, **649**, A3
- Rivinius, T., Carciofi, A. C., & Martayan, C. 2013, *A&ARv*, **21**, 69
- Robitaille, T. P., Meade, M. R., Babler, B. L., et al. 2008, *AJ*, **136**, 2413
- Rybizki, J., Green, G. M., Rix, H.-W., et al. 2022, *MNRAS*, **510**, 2597
- Schmidt, E. G., Johnston, D., Langan, S., & Lee, K. M. 2004, *AJ*, **128**, 1748
- Shridharan, B., Mathew, B., Nidhi, S., et al. 2021, *RAA*, **21**, 288
- Stapper, L. M., Hogerheijde, M. R., van Dishoeck, E. F., & Mentel, R. 2022, *A&A*, **658**, A112
- Steinmetz, M., Guiglion, G., McMillan, P. J., et al. 2020, *AJ*, **160**, 83
- Taylor, M. B. 2005, in ASP Conf. Ser. 347, Astronomical Data Analysis Software and Systems XIV, ed. P. Shopbell, M. Britton, & R. Ebert (San Francisco, CA: ASP), **29**
- Thé, P. S., de Winter, D., & Perez, M. R. 1994, *A&AS*, **104**, 315
- Torra, F., Castañeda, J., Fabricius, C., et al. 2021, *A&A*, **649**, A10
- Valegård, P.-G., Waters, L. B. F. M., & Dominik, C. 2021, *A&A*, **652**, A133
- van den Ancker, M. E., Gentile Fusillo, N. P., Haworth, T. J., et al. 2021, *A&A*, **651**, L11
- van der Marel, N., & Mulders, G. D. 2021, *AJ*, **162**, 28
- van der Marel, N., Birnstiel, T., Garufi, A., et al. 2021, *AJ*, **161**, 33
- Vieira, S. L. A., Corradi, W. J. B., Alencar, S. H. P., et al. 2003, *AJ*, **126**, 2971
- Villebrun, F., Alecian, E., Hussain, G., et al. 2019, *A&A*, **622**, A72
- Vioque, M. 2020, PhD thesis, University of Leeds, <https://etheses.whiterose.ac.uk/27872/>
- Vioque, M., Oudmaijer, R. D., Baines, D., Mendigutía, I., & Pérez-Martínez, R. 2018, *A&A*, **620**, A128
- Vioque, M., Oudmaijer, R. D., Schreiner, M., et al. 2020, *A&A*, **638**, A21
- Vorobyov, E. I., Elbakyan, V., Hosokawa, T., et al. 2017, *A&A*, **605**, A77
- Wichittanakom, C., Oudmaijer, R. D., Fairlamb, J. R., et al. 2020, *MNRAS*, **493**, 234
- Wisniewski, J. P., Berdyugin, A. V., Berdyugina, S. V., et al. 2021, arXiv:2111.06891
- Wright, C. O., Egan, M. P., Kraemer, K. E., & Price, S. D. 2003, *AJ*, **125**, 359
- Zhang, Y.-J., Hou, W., Luo, A.-L., et al. 2022, *ApJS*, **259**, 38